EUROPEAN ORGANIZATION FOR NUCLEAR RESEARCH

CHANNELING OF PROTONS, PIONS, AND DEUTERONS IN THE GeV REGION

H. Esbensen, O. Fich, J.A. Golovchenko, K.O. Nielsen,
E. Uggerhøj and C. Vraast-Thomsen

Institute of Physics, University of Aarhus,
Aarhus, Denmark

G. Charpak, S. Majewski*) and F. Sauli

CERN, Geneva, Switzerland

J.P. Ponpon

Centre de Recherches Nucléaires, Strasbourg, France

Geneva - 21 February 1977

(Submitted to Nuclear Physics B)

*) On leave from Institute of Experimental Physics, Warsaw University, Warsaw, Poland.

Abstract

Strong directional effects have been observed when 1.15 and 1.35 GeV/c protons, π^+ and π^-, and deuterons penetrate through germanium crystals. Transmission, wide-angle scattering, and an attempt to do blocking distributions are obtained from experiments using position-sensitive drift chambers. Corresponding measuremnts of energy loss in germanium crystals are also presented. These experimental results are compared to theory for energy loss, and satisfactory agreement is obtained.

1. Introduction

Strong directional effects have been observed for a variety of very energetic, charged heavy particles penetrating through a single-crystal material. The probability of large-angle scattering and transmission into forward directions are seen to depend dramatically upon the relative orientation of the crystal and particle beam, with positive and negative particles behaving differently. The ionization energy-loss distributions have also been measured, and they also exhibit strong directional effects associated with penetration through crystalline matter. (Some preliminary results may be found in refs. [1-3].)

Such effects have previously been studied in detail for charged heavy particles with energies $\leqslant$ 10 MeV and for electrons and positrons with energies up to 1 GeV, and here ref. [4] contains a comprehensive review.

The case of crystal penetration by nonrelativistic positively charged, heavy particles has been described theoretically by Lindhard[5]. This theory, based upon a classical description of the motion, predicts that when the incident beam enters a crystal at a small angle to an axial or planar direction, a strong correlation in successive collisions results, which serves to gently deflect most of the particle paths away from the high-density strings and planes of atoms. Consequently, under such channeling conditions, a general suppression of all processes requiring small impact parameters is expected. Experimentally, this reduction in yield has been observed for wide-angle Rutherford-scattering, nuclear reactions, inner-shell excitation, the related energy loss, and x-ray production.

The present work may be viewed as the beginning of the natural extension of heavy-particle channeling studies from the low- to the high-energy

region. In addition to simply extending the energy range of particles already studied in previous channeling experiments, interesting possibilities are created by new species of particles available for investigation. For example, the observation of π^+ and π^- channeling behaviour serves to elucidate the discriminatory manner in which the crystal interacts with positive and negative particles. Previously, only electrons and positrons have been used in such studies. In these cases, the small mass of the penetrating particles leads to the well-known diffraction effects associated with coherent scattering from many lattice atoms. The importance of multiple coherent scattering, associated with many crystal reciprocal lattice vectors together with inelastic effects from electron and nuclear recoil, can make an overall quantal description of energetic electron and positron penetration quite complex. It is interesting that, under appropriate conditions, many aspects of this problem can be understood from a classical view of the motion[5]. A comparison of positron- and proton-channeling aspects at energies around 1 MeV shows, after a relativistic scaling, a very striking agreement, and from these results it can be concluded that for 1-MeV positrons, quantal corrections to the classical picture are small for channeling along a strong axis[6].

Also electrons behave classically at relativistic energies. Here a study of emergent β^- and β^+ emitted from ^{64}Cu implanted in a copper crystal also demonstrated a very pronounced difference in crystal penetration by positive and negative particles[7]. Still, particularly for the case of energetic electrons, a comprehensive description seems lacking, and the extension of experimental knowledge to include other available particles, such as negative hadrons and muons produced in high-energy accelerators, is natural.

Finally, we would like to draw attention to the experimental approach utilized in this experiment since it is somewhat unconventional compared with

the methods used in lower-energy channeling investigations. A set of position-sensitive drift chambers placed in front of and behind the sample under study has allowed simultaneous investigation of a relatively wide range of incident and exit angles. This manner of operation has permitted the experiment to be performed in a poorly collimated beam. In fact, by using the large angular spread of the beam, we obtain a broad angular map of the channeling effects which eliminates the need for prior extremely fine angular alignment of the crystal with accurate remote-controlled, small-angle goniometers.

2. General Description of Channeling Phenomena

2.1 Positive particles

The conceptual framework used to describe the channeling effect has existed for about ten years, during which time various aspects of the phenomena have been studied in great detail. The main interest has centered on crystal penetration of protons, alpha particles, and heavier ions with energies of the order of MeV/nucleon. The description of the observed directional effects generally relies upon a classical model for the particle motion inside the crystal. For positive particles, the theoretical analysis may be carried quite far. The basic work here is ref. [5], where the classical description is justified and the more important notions established. The following discussion will be based mainly upon this analysis.

The critical angle ψ_1 is the basic quantity determining the conditions under which channeling effects will be important. When positive particles enter a crystal at angles smaller than ψ_1 relative to low-index axial directions, their subsequent trajectories in the target are strongly effected by correlated collision sequences with atoms on this string. A similar situation has occurred for positive particles exiting the crystal within such angles. For an axial case,

the critical angle for relativistic particles is given by refs. [7] and [8],

$$\psi_1 = \sqrt{4Z_1Z_2e^2/(pvd)} \quad , \tag{1}$$

where Z_1e and Z_2e are the nuclear charges of the incident particle and the target nuclei, respectively, p and v are the relativistic momentum and velocity of the incident particle, and d is the distance between target atoms along the strings of atoms in the axial direction. An analogous result[9] for penetration near planar directions may be found as

$$\psi_p = \sqrt{4Z_1Z_2e^2Nd_pCa/(pv)} \quad . \tag{2}$$

Here, N is the atomic density of target atoms, d_p is the distance between atomic planes, C is a constant of order of $\sqrt{3}$, and a is the Thomas-Fermi screening length for the combination Z_1, Z_2 ($a=0.885\, a_o/(Z_1^{2/3} + Z_2^{2/3})^{1/2}$) . In the following, however, we shall discuss mainly the case of axes.

Equations (1) and (2) usually appear in a nonrelativistic form with the factor $\frac{1}{2}pv$ replaced by the nonrelativistic kinetic energy E . Use of the former factor when $v \to c$ follows simply from the impulse-approximation calculation of the individual small scattering angles determining the channeling trajectories.

Figure 1a illustrates how, for positive particles satisfying the above channeling conditions, a remarkably stable motion can result, whereby successive small-angle screened Coulomb collisions with target atoms tend to keep the fast particle away from the high atomic-density strings of atoms. Moreover, the correlations that the crystal lattice supplies to small-angle deflections result in an approximately conserved quantity, the transverse energy $E_\perp$. That is, if the particle motion is analyzed, the quantity

$$E_\perp = \tfrac{1}{2}pv\varphi^2 + \frac{1}{d}\int_{-\infty}^{\infty} dz V(\sqrt{r^2+z^2}) \equiv \tfrac{1}{2}pv\varphi^2 + U(r) \tag{3}$$

will be approximately independent of the point on a chosen trajectory. Here, φ is the instantaneous angle between the particle motion and the string direction, while r is the corresponding distance to the string. Thus, except for the presence of the relativistic mass in the definition of p, the first term on the right-hand side of eq. (3) is like a nonrelativistic kinetic energy of the motion transverse to the string direction. V is the interatomic potential energy function, and thus the continuum potential $U(r)$ in eq. (3) represents a kind of transverse potential energy obtained by averaging V along the string direction. Evidently, the compound correlated small-angle scattering leads to a separation of the motion parallel and perpendicular to the string direction. The motion perpendicular to the strings, projected on a plane transverse to the string direction, is shown in fig. 1b. The role of the repulsive string potential in creating a forbidden region close to the string of atoms is clearly seen in fig. 2, where a sequence of string collisions in the transverse motion is depicted. Trajectories with small $E_\perp$ will stay quite far away from the strings of atoms, while those with increasing $E_\perp$ may penetrate closer to the strings. Thus, for trajectories with $E_\perp \geq \frac{1}{2} pv\psi_1^2$, penetration will be possible so close to the string that the resulting large scattering angles will destroy the channeling effect (see trajectory labelled 2 in figs. 1a and 3 in fig. 2). $E_\perp$ will, in fact, then not be conserved, and such trajectories are called part of the <u>random beam</u>. Those trajectories with $E_\perp \leq \frac{1}{2} pv\psi_1^2$ are in the <u>aligned</u> or <u>channeled beam</u>. (Both types of trajectory are shown in figs. 1a and 2.) Note also from fig. 2 that channeled particles are not usually trapped in the "channels" formed by the strings.

To determine the transverse energy of a particle entering the crystal from an external beam, one simply adds the external transverse kinetic energy to the continuum potential energy at the point of entry in the transverse plane. Since

the transverse continuum potential (i.e., the second term on the right-hand side of eq. (3)) is small over most of the transverse space, it follows that most particles, upon entering the crystal, will be part of the channeled beam for angles of incidence relative to the axis $\leqslant \psi_1$ and part of the random beam for angles of incidence $\geqslant \psi_1$. Within the above idealized model, particles do not move from the channeled to the random beam and vice versa as they propagate through the crystal.

Deviations from the above continuum description, i.e., nonconservation of transverse energy for channeled particles, result mainly from multiple scattering on electrons and from thermal vibrations in the target material. The statistical accumulation of these effects also tends to destroy the channeling effect, i.e., they cause dechanneling. Discussion of the influence of dechanneling is carried out in sec. 3.9.

There may be some readers who feel uncomfortable about the use of classical pictures to describe the compound Coulomb scattering effects at high energies, which lead to channeled motion. It is indeed true that in a single Coulomb collision, such that $\varkappa = Z_1 Z_2 e^2/\hbar v < 1$, the uncertainty principle makes meaningless the concept of impact-parameter-dependent scattering angles[10]. This result is strictly applicable for an isolated Coulomb collision. The important point for channeling is that an entire string collision must be analyzed to determine whether classical pictures apply. In contrast to what is the case for an isolated collision, the result is obtained that classical pictures are meaningful in heavy-particle channeling studies, even for $v \to c$ (see Refs. [5] and [8]).

We now briefly discuss two basic methods of observing channeling experimentally, viz. by transmission and by wide-angle scattering experiments. We attempt to relate the observed results to the notions mentioned above.

Transmission experiments. The geometry of an idealized transmission experiment is shown in fig. 3a. The detector is placed so as to accept particles that have been barely deflected upon passing through the crystal. The transmission yield is then measured as a function of the angle θ between crystal axis and beam.

For angles of incidence far from an axial or planar direction, the emergent distribution of angles is essentially determined by random multiple-scattering processes, and for large θ, the yield measured on the detector therefore corresponds to the maximum of the multiple-scattering distribution.

For angles of incidence aligned within ψ_1 of an axis, the great majority of particles will acquire transverse energies on entering the crystal such that they will be in the channeled beam. Here the random multiple-scattering process is strongly suppressed, and if the crystal is not too thick (i.e., dechanneling effects are small), most of these particles will leave the back side of the crystal with transverse energies satisfying the channeling conditions and will thus emerge within angles of order ψ_1 of the axis. With the velocity component of particle motion along the axis direction essentially unchanged, the angular distribution of the transmitted channeled particles is determined by the transverse velocity distribution at the back side of the crystal. Therefore, if ψ_1 is smaller than the root mean-square random multiple-scattering angle associated with the sample thickness, a strong increase in the yield appears under channeling conditions (as illustrated in fig. 3a).

Wide-angle scattering experiments. Here, on the other hand, one observes the probability of a small impact-parameter interaction (i.e., wide-angle scattering) as a function of the angle of incidence θ_i (see fig. 3b). This probability clearly depends upon the flux of penetrating particles near the strings

of atoms. The wide-angle scattering yield is usually measured relative to the yield observed for angles of incidence far away from any axis and planar directions. Only particles in the random beam or particles with transverse energies large enough to allow penetration to within the thermal vibrational amplitude of the strings can contribute to the scattering yield. At shallow depths in the crystal (i.e., prior to the onset of dechanneling processes), when the incident beam is perfectly aligned with a low-index axis, these particles amount to only a few percent of the total incident beam. Thus, wide-angle scattering is reduced by one or two orders of magnitude relative to random penetration. This minimum yield (χ_{min}) results in the first approximation from those particles in the incident beam that hit the crystal within a distance $\sim\rho$ from the string, where ρ is the root mean-square amplitude of atomic vibrations perpendicular to the string. From this results $\chi_{min} \simeq Nd\pi\rho^2$ (Nd is the number of strings per unit area). If the angle of incidence to the axis is increased, the transverse kinetic energy of the beam at the front surface of the crystal is increased so that the distribution of transverse energies in the crystal is weighted towards larger values. A corresponding increase in the probability to be near the string results in increasing wide-angle scattering yield χ. The experimentally observed angle required for the yield to increase from its minimum value χ_{min} half the way towards the random value is $\psi_{1/2}$. Values of $\psi_{1/2}$ are expected to be about 75% of ψ_1 at shallow depths (see ch. 4). We emphasize that due to dechanneling effects, the yield χ is a function of depth of penetration into the crystal. Thus the minimum yield χ_{min} increases at greater depths as dechanneling processes accumulate.

Blocking experiments. Here, one looks at the distribution of angles of charged particles exiting the crystal when the trajectories of the particles are known to pass close to or originate from the string. Such particles may either

result from a small impact-parameter interaction (i.e., wide-angle scattering) with a string atom or originate as reaction products emitted from radioactive nuclei sitting in a lattice position. In both cases, the charged particles have a small probability of leaving the crystal along the axial direction. The blocking effect is easily understood in terms of the shadowing effect of the string on such particles, whose trajectories would otherwise have exited near the string direction (see trajectory 3 in fig. 1a).

As shown in fig. 3c, the experimental situation for a blocking experiment can be closely related to the wide-angle scattering experiment. By a reversibility argument, it has been shown[5] that the angular yield in the blocking effect should be identical to the wide-angle scattering yield previously discussed if energy loss may be neglected for the trajectories connecting the external beam (either entering or exiting) with the position of the scatterer in the crystal. This result is based upon the fact that the probability of hitting a lattice atom for a particle incident on a crystal in a specific direction is equal to the probability for the particle to escape from the crystal, in that direction, when emitted from the lattice atom. The probabilities are here taken relative to the case of an amorphous target. The equivalence has been observed experimentally for α particles and protons in the MeV region[11].

2.2 Negative particles

Up to now, experimental investigations of channeling phenomena for negative particles have mainly been restricted to channeling of electrons of up to 20 MeV. Wide-angle scattering as well as blocking and transmission experiments have been performed. Also the rule of reversibility is shown to hold (for a survey, see ref. [4]). Qualitatively, for high-energy electrons, the main features of the experimental results may be anticipated from classical considerations on

electron trajectories inside the crystal, with quantal interference effects accounting for diffraction wiggles within the classical envelope of the angular distributions. Thus, one may imagine a continuum potential representing the average attraction of the electron to the atomic strings that is equal in magnitude but opposite in sign to that for singly charged, positive particles. This attraction suggests that when the negative particles are aligned near to major crystallographic axes, an increase in small-impact parameter interactions, such as wide-angle scattering and blocking, will result. It would also seem reasonable to expect that this increased scattering would result in dips in the forward-transmission yield for thin crystals. (As shown in fig. 3a, positive particles give a transmission peak under similar conditions.)

In the wide-angle scattering results given in ref. [12], this increase in scattering yield and the dip in the forward-transmission yield is certainly observed.

In the electron-transmission experiments of refs. [13,14], dips are observed in transmission that correspond to the enhanced scattering when the beam direction becomes almost parallel to a major axis. Narrow peaks inside the broader dips were also observed in these experiments. It has been proposed[13] that the structure of these peaks is due to trajectories bound to the strings in transverse space but having such a high transverse angular momentum that penetration close to the atomic strings does not occur. The resulting stable motion with the electrons spiralling around the positive strings leads to high transmission probabilities through the crystal. For a perfectly aligned external beam, no trapped high angular momentum states would exist, and the peak in transmission should then be expected to have a narrow dip inside it. This has also been observed recently (ref. [14], fig. 1).

Theoretically, channeling effects for MeV electrons have been described by both classical approximation and many-body theory (for a review, see

refs. [15] and [4]). The results of these calculations are in reasonably good agreement for the transmission patterns as well as for wide-angle scattering phenomena. For high-energy negative particles, no such calculations exist. Concerning energy loss of channeled negative particles, neither theoretical calculations nor experiments have been performed so far, not even for MeV electrons.

The general description of channeling phenomena given in this chapter is based upon a simplified and schematic experimental setup, see fig. 3, with well-collimated beams and goniometer for crystal alignment relative to the beam or detector. In our high-energy channeling experiments, quite a different technique is used. Here, the crystal orientation is kept fixed during an experiment, while a set of high-accuracy drift chambers determines the incoming and outgoing beam angles.

3. Experimental Setup and Procedure

Having described the main features of channeling phenomena, we now proceed to describe the experimental techniques we have used to extend measurements to the high-energy region. Also the main principles for the experimental procedure will be given as a background for a presentation of the experimental results obtained.

3.1 General layout

The experimental apparatus was installed in a test beam of the CERN 30 GeV/c proton synchrotron. The schematic layout of the experiment can be seen in fig. 4. The beam itself was a low-intensity (around 10^4 particles/cm^{2}sec) secondary nonseparated charged beam with a momentum adjustable between 1.0 and 1.5 GeV/c. In the positive polarity, it contained roughly equal amounts of protons and π^+ with about 1% of deuterons, while in the opposite polarity it con-

tained essentially only negative pions. We have normally used a large momentum byte of ±4% and a divergence at the focus of ±5 mrad in the vertical plane and ±8 mrad in the horizontal plane.

When running in the positive polarity, the discrimination between deuterons, protons, and pions was done by measuring the time-of-flight between two scintillation counters (SC1 and SC5 in fig. 4) about 4 m apart. Three additional scintillation counters, SC3 in coincidence and SC2, SC4 in anticoincidence, were used to define the usable fraction of the beam so that the beam spot at the goniometer did not exceed the maximum size of the crystal.

The incident as well as the exiting particle trajectories were measured by a set of six position-sensitive drift chambers, DC1 to DC6. Helium bags in the front arm and a vacuum chamber in the back arm helped to reduce multiple scattering, which was the main factor limiting our angular resolution (see fig. 4). The goniometer, mounted in the vacuum chamber, allowed an adjustment of the crystal axis to the average beam direction, although a precise alignment was not necessary due to our method of measurement (see sec. 3.6). The energy-loss experiments required cooled crystals, and for this purpuse, a liquid-nitrogen cooling system was added to the goniometer.

3.2 Position-sensitive detectors

The basic principle of the experiment was to record, for each beam particle obeying the simple geometrical constraints already described, both the incident and the exiting angle on the crystal and then to disentangle the interesting features of the angular distributions by an off-line data analysis. For this purpose, we have used a set of high-accuracy drift chambers to record, on each event, the two-dimensional coordinates of the tracks on selected planes (DC1 to DC6 in fig. 4). The detailed behaviour of drift chambers has been de-

scribed elsewhere[16], but we report here the basic principle of their operation. An insulating frame supports two sets of parallel, thin conductive wires, which are maintained by means of an external resistor divider at a linearly decreasing potential, as shown in fig. 5. This geometry creates a gaseous region, the drift space, of constant electric field. At one end of the region, a thin anode wire maintained at a positive potential acts as a proportional counter. When an ionizing, charged particle crosses the drift region, the leftover electrons migrate against the field and eventually reach the proportional-counter section where, by avalanche multiplication, their arrival can be detected at a time t_1. The time zero t'_o for a position-sensitive detector is calculated from the time t_o for a particle crossing the scintillation counter SC1, see fig. 4, plus the time-of-flight to the detector in question. The coordinate s, see fig. 5, is

$$s = \omega(s) \cdot (t_1 - t'_o) \quad , \tag{4}$$

where $\omega(s)$ is a known function representing the drift velocity.

Drift chambers are 6 mm wide and are normally operated at atmospheric pressure in an open flow of gas; this allows the use of very thin mylar windows. Typical drift-wire diameter is 0.1 mm with a spacing of 1 mm. The anode-wire diameter is normally only 20 μm in order to obtain a stable high-gain operation. Electro-negative impurities must be carefully avoided. The gas mixture recommended in ref[16] (67.0% argon, 30.5% isobutane, 2.5% methylal) is used, having the peculiarity of providing a drift velocity of about 5 cm/μsec, independent of the electric-field value above a certain field; in these conditions, also the variation of the velocity with other parameters (pressure, temperature, gas composition, etc.) is greatly reduced. For a given particle flux, there is a limit to the maximum cell length if one wants to avoid multiple-event recording. For this experiment, a 25-mm drift space was both necessary and sufficient for DC1,

DC2, and DC3, resulting in about 500 nsec maximum drift time.

If a larger surface of detection is necessary even with a short drift time, a symmetric structure can be constructed like that shown in fig. 6, where the single anode is replaced by a couple of close wires acting as independent counters. The basic cell can be repeated at will, the auxiliary field wires serving the purpose of creating a sharper separation between adjacent cells. Chambers DC4, DC5, and DC6 (see fig. 4) were of this kind with three pairs of anode wire on each plane, covering an active surface of 150x150 mm^2.

The two-dimensional detector is obtained by mounting at each drift-chamber position two of the described modules rotated 90° with respect to each other; the two planes can be mounted in the same gas enclosure, although an electrostatic screening consisting of a 10 μm thin metal foil between adjacent modules is necessary.

Owing to the diffusion in the gas during the process of migration of the electrons, the accuracy that can be obtained in a drift chamber depends slightly on the drift length, as shown in fig. 10 of ref. [16]. All our data are consistent with a long-term average accuracy below 100 μm (standard deviation) in running conditions for each coordinate measurement. At the beam energy available for the present experiment, the multiple-scattering contribution to the final angular resolution is larger than that computed solely from the drift-chamber accuracy, and the results for exiting tracks are given in table 1.

Due to increased multiple scattering and to certain geometrical constraints, the overall instrumental resolution for the incident tracks is a factor of two worse than that for the exiting tracks in table 1. It must be noted that it is rather difficult to determine experimentally the overall resolution, and the numbers given in table 1, based upon calculated estimates of the multiple scattering, are only approximate.

3.3 Crystal preparation

The selection of suitable crystal samples for high-energy channeling experiments requires some care. Many so-called 'single crystals' have a large mosaic spread, i.e., they are in fact made up of small crystallites with relative orientations distributed over a range of angles that can be of the order of several mrad. Equations (1) and (2) suggest that critical angles smaller than 1 mrad will be encountered, and thus in such crystals, the observed channeling effects would be substantially "smeared out" and difficult to detect at all. There exists, however, a class of crystalline materials, well-known for their high quality in this respect from dynamical x-ray-diffraction studies. Device-quality semiconductor materials belong to this class. We chose germanium because its high atomic number should result in large scattering angles and energy loss. Furthermore, the technology of making intrinsic ionization detectors from this is well established. The germanium material, from which our crystal (non-detector) samples were prepared, was tested by x-ray anomalous transmission and etch-pit count and showed a mosaic spread of at most 10^{-2} mrad and a dislocation density of $\sim 100\ cm^{-2}$. From a practical standpoint, the samples were therefore perfect.

All crystals were cut so that the $\langle 110 \rangle$ direction was within a few mrad of the surface normal, and a few tenths of a millimeter was etched away to remove damage from the sawing.

The energy-loss measurements were performed by using an intrinsic germanium detector[17] as a crystal target. In order to avoid permanent storage at liquid-nitrogen temperature and to ensure good charge collection of the carriers (i.e., no trapping of the radiation-generated electron-hole pairs), high-purity material (net impurity concentration $\sim 3 \times 10^{10}$ atoms/cm^3) was used so that the detector had to be cooled only during measurements. Two main problems arose in

the fabrication of the detectors: The first was to find a front contact providing a thin entrance window, resulting in a minimum amount of multiple scattering. The second was to avoid a high-temperature treatment so as to prevent penetration of fast-diffusing impurities into the crystal. These requirements were fulfilled by using a low-energy (15 keV) implantation of boron ions to make the front-rectifying contact on N-type, high-purity germanium and a deposition of a thin (200 Å) aluminium layer as a back contact. A $10^{14}/cm^2$ boron dose was sufficient to provide, without any annealing, good electrical conductivity. Further, the low implantation energy and dose of light ions resulted in a minimum of damage in the crystal and an entrance window of $\sim$ 2000 Å, which conserved the same crystalline structure as the bulk. A grooved structure around the implanted layer was used to reduce the leakage current. The detector, which was 0.67 mm thick, was totally depleted at the operation voltage used (15 V).

During experiments, the detector was cooled to 100 K in the sample goniometer and connected to a charge-sensitive preamplifier, which supplied an energy pulse to a selectable filter amplifier (shaping time 4μs) for the recording of the energy-loss spectra and a timing pulse used in coincidence with the other detectors. The energy resolution of the detector was $\sim$10 keV.

3.4 Data acquisition and data handling

A schematic diagram of the on-line electronic data-acquisition system is shown in fig. 7. The incoming-beam tracks are individually detected by five scintillation counters, SC1 to SC5 (fig. 4), and the photomultiplier output is discriminated and shaped. A "good" event is defined by the logic coincidence $SC1.\overline{SC2}.SC3.\overline{SC4}.SC5$, which selects the beam track that hits the sample crystal and is contained in the active region of the drift-chamber setup. The pulse widths and timings are arranged in such a way that the coincidence output has the time t_o of SC1, i.e., is independent of the time-of-flight. A timed, nar-

row coincidence between SC1 and SC5 allows selection between particles having different velocities by a proper setting of the relative delay between the two signals. In the master coincidence, the two logic functions are combined to obtain both the time reference t_o and the READ command for the data transfer. On each event, a set of CAMAC standard time-to-digital (Lecroy type 2228 Octal TDC) converters is started at the time t_o and, as shown in the diagram, the drift times for each drift-chamber anode wire are recorded. Our actual setup consisted of 32 identical TDC channels, all having 1 nsec channel width and 1 μsec range. An additional TDC channel with higher sensitivity is used to record the actual time-of-flight.

When running with a crystal detector, the pulse height is recorded by an analogous-to-digital converter (ADC), see fig. 7.

Some additional units, not shown in the diagram, were also used to scale the scintillation counters and the event rates. The READ command from the master coincidence then initiates the READ sequence that transfers the event block to a small on-line computer (HP-2100A). In the data-taking operation, all events are recorded on tape. The analysis of the data is performed off-line on a more powerful computer. Standard procedures were used before each run to ensure a correct behaviour of the drift-chamber detectors as well as of the associated electronics, and to calibrate the individual TDC-conversion slopes and off-sets. The counting rates were limited to ~120 counts/bursts with one burst every 2.5 sec.

3.6 Data reduction

For each drift-chamber plane, the coordinate of the track crossing point was obtained by multiplying the channel number given by the corresponding TDC by a constant, taking into account both the converter slope and the drift velocity. The relative position of the detectors, not known *a priori* with the required

accuracy (below 100 μm), was then obtained by a straight-line, best-fit procedure. Before each run, a special tape was recorded with the sample crystal removed so as to reduce the multiple scattering and allow the alignment of the two sets of chambers. Only events producing a single hit in all planes were accepted in the reconstruction, and a rough alignment condition was verified separately in the front and back detectors for each track. The angle of incidence of the track on the crystal was then computed from the difference in the coordinates of DC1 and DC3. The intersection of the incident track with the crystal was also computed and the event accepted for genuine encounters. Typically, 60% of the raw events on tape satisfied the above acceptance criteria, which provided an average number of 200 000 valid events per magnetic tape. Thus, the magnetic tapes contain all information about the impinging and exiting beam particles. From them, scattering angles may be computed and incident and exiting angular distributions constructed where constraints on scattering angles, energy loss, or position on the target may be imposed, as described in the next section.

3.6 Crystal alignment

Since the channeling angles involved in high-energy experiments are quite small, crystal alignment can be a rather tedious undertaking when performed in the manner commonly used at lower energies. There one generally has a well collimated incident beam, and the detailed, time-consuming tilting scans with the crystal goniometer are required to find and investigate channeling effects near axial or planar directions. In our case, we were able to perform transmission experiments by using the large-divergence incident beam, coupled with the position-sensitive drift chambers, and thus obtained at the same time an entire angular map of channeling effects. It was therefore only necessary to align the crystal axis (plane) of interest within this broad distribution of incoming angles.

Figure 8 shows a plot of the incident angular distribution of those pions that have been scattered through angles smaller than 0.35 mrad (see sec.4.1). For the data shown in fig. 8, the beam momentum was 1.15 GeV/c and the crystal thickness 1 mm. It is clearly seen that for incidence parallel to the ⟨110⟩ axis and the {111} and {110} planes, a pronounced increase in intensity is found. When the crystal was positioned with the ⟨110⟩ direction outside the beam cone, the geometry of the observed planar effects indicated the direction and magnitude of the goniometer tilt required to obtain results like those of fig. 8. The very pronounced planar effects have turned out to be completely essential for aligning the samples. The angles between the planes in the stereographic plot given in fig. 8 are found to be in agreement with those expected from crystallographic considerations.

Such a stereogram can be used to choose different scan geometries in order to obtain detailed information about the intensity distribution around the axes and planes. Thus, the dashed line in fig. 8 is a scan direction across an axis away from major planes. A typical region for planar scanning is also indicated. Here the scanning direction is perpendicular to the planes. It is worth mentioning that although the planar effects are weaker than are axial effects, it is possible under certain conditions to improve the statistical accuracy by integrating in strips parallel to the planes (see fig. 8).

3.7 Random-beam alignment

Before discussing our channeling results, we present briefly a preliminary experiment for measuring the random multiple scattering when the crystal is oriented such that no major axes or planes fall within the incident-beam cone. Plotted in fig. 9 is the distribution of scattering angles of all incident-beam particles in the 0.67 mm thick sample with 1.35 GeV/c π^+ .

As expected from the treatment of random multiple scattering by Williams and Bohr[10], the distribution can be divided into a central Gaussian part, which results from small-angle multiple scattering, and at large angles a tail mainly due to single scattering events. The solid curve in fig. 9 is a Gaussian distribution,

$$P(\theta)d(\theta^2/\theta_G^2) = C \cdot \exp(-\theta^2/\theta_G^2)d(\theta^2/\theta_G^2) \quad , \tag{5}$$

fitted to the data with $\theta_G = 2.30$ mrad. The theoretically expected value of θ_G due to multiple scattering in the target is determined from the implicit equation,

$$\theta_G^2 = 8\pi(Z_1 Z_2 e^2)^2 NR \ln(\frac{pa\theta_G}{\hbar})/(pv)^2 \tag{6}$$

to be $\theta_G = 2.16$ mrad. Here, Z_1 and Z_2 are the atomic numbers of the projectile and the target, respectively, p and v are the beam momentum and velocity, N is the density of target atoms, a is the Thomas-Fermi screening length, and R is the crystal thickness.

Equation (6) reflects the idea that the mean-square scattering angle θ_G^2 of the Gaussian part is determined by scattering events through angles smaller than θ_G. When account is taken of angular resolution of incidence- and exit-angle determinations of the track (discussed in sec. 3.2), agreement between theory and experiment is within 5%. These results establish the overall reliability of the experimental apparatus and procedure.

3.8 Normalization

In order that our channeling results should not contain intensity variations due to incident-beam angular distribution, it is necessary to normalize the data. This was accomplished for both the transmission and the wide-angle scattering experiments discussed below by dividing the angular space occupied by the incident beam into a 60×60 array of solid-angle elements. The i'th element,

from which each event originates, is determined and the event is given a weight $1/n_i$, where n_i is the total number of incident particles in that element.

3.9. Selection of crystal thickness

Since dechanneling restricts our choice of crystal thickness, it was necessary beforehand to estimate this influence.

Lindhard[5] has proposed a method of calculating the angular yields as a function of depth, based upon the continuum model with transverse energy, nonconservation being determined by a diffusion model. The diffusion of transverse energy is governed by a diffusion function that is dependent on transverse energy. The diffusion function contains contributions from multiple scattering by both electrons and thermal vibrations. Bonderup et al.[18] have made detailed calculations by this method for 2-MeV protons in silicon and have obtained satisfactory agreement with experiment.

We have used this method with slight modifications to include relativistic effects in the multiple-scattering-dependent diffusion function. This is mainly accomplished by replacing the rest mass appearing in the nonrelativistic formulas with the relativistic mass $m_o/\sqrt{1-v^2/c^2}$. Figure 14 shows the result of this calculation. The average yields are given for several assumed crystal thicknesses for incident protons of 1.15 GeV/c. For 1-mm thick crystals, an average minimum yield of 10% is obtained, and we therefore expect to observe strong channeling effects for the crystal mentioned in sec. 3.3.

4. Results and Discussion

Based on the apparatus and procedure described in ch. 3, the following four types of channeling experiments are accomplished: (i) Transmission experiments, (ii) Wide-angle scattering experiments, (iii) Attempt to do blocking, and finally (iv) Energy-loss measurements. Each experiment is discussed and analyzed within the framework of the presentation of channeling phenomena given in ch. 2.

4.1 Transmission experiments

Under the restricted conditions of our experiments, i.e., obtainable angular resolution and beam intensity, it became evident at an early stage that the easiest way of detecting the channeling effect would be via transmission experiments.

Compared to the schematic experimental setup illustrated in fig. 3a, the following modifications were made to suit our experimental conditions: The collimation requirement that only particles transmitted in the forward direction be detected is replaced by the condition that a given event is accepted if the difference between its incident and exit angle is less than a cut angle α, independent of the incident direction within the broad beam divergence the event occupies. The angle α should not be smaller than the angular resolution for the difference between incident and exit angles. Too small a choice of α also limits the statistical accuracy of the results. A value of $\alpha = 0.35$ mrad was chosen.

Then, instead of obtaining data for different tilt angles of the crystal (see fig. 3a), we simply determine the incident angles from which the above accepted events originate. Since events may come from anywhere within the broad beam divergence, we obtain a broad angular map of the small-angle transmission channeling effects. Figure 8 shows such a normalized map, containing the axial and planar information of interest. Such transmission distributions have been obtained for π^+, protons, and deuterons with a crystal thickness of 1 mm and a momentum of 1.15 GeV/c. Below we present only the axial and planar scans from these overall distributions. For π^-, only axial scans are presented. Here the beam momentum was 1.35 GeV/c and the sample was 0.67 mm thick.

Axial transmission. In order to present a detailed measurement of the intensity distribution near the ⟨110⟩ axis, a scan across the axis away from major planes was made (fig. 8, dashed line).

Figure 10 shows axial scans for π^+, protons, and deuterons as a function of the angle between the exit direction from the crystal and the ⟨110⟩ axis. The intensity distributions show an increase in the transmission yield of about a factor of 10 for those particles in the beam that are parallel to the ⟨110⟩ axis. It is seen that π^+, protons, and deuterons give practically the same intensity distributions concerning peak height and FWHM. For deuterons it should be noted that due to low beam current, the statistical uncertainty and angular resolution are worse than for π^+ and protons.

The channeled peak-to-nearest background has a value of about 10 for all three types of particle. For the experimental setup with a poorly collimated beam, a theoretical evaluation of the peak-to-background ratio is difficult. Furthermore, dechanneling effects and finite angular instrumental resolution also contribute to the uncertainty. We therefore refrain from a detailed analysis of these data.

The transmission distribution for π^- around the ⟨110⟩ axis is shown in fig. 11. The random value is determined by averaging over many events far from the axis direction. A broad dip going down to 50% of the random value and extending over an angular range of ~ 8 mrad FWHM is obtained. The distribution also clearly has a peak in the centre. It should be noted that the data at large angles show greater uncertainty due to low incident-beam intensity in this region.

Our π^- transmission results are qualitatively very similar to those observed for electrons, as described in sec.2.2, although the height of the central

peak is greater than in any observation with electrons. The central peak could well contain another narrow dip that is obscured by multiple scattering due to excessive crystal thickness or angular resolution of the detector. An added piece of information is contained in the energy-loss results of fig. 19 of those π^- in the peak of the transmission yield. This loss distribution is quite similar to the random one. One can be quite sure then that the trajectories associated with these particles are not primarily sampling low electron-density regions of the transverse space. Indeed, the kind of trajectories that have been proposed to explain the transmission peaks[13] undergo a spiralling rosette motion around the string with the particle spending most of its time in regions of intermediate electron density and energy-loss rate several Thomas-Fermi screening lengths from the string. The high energy-loss-rate trajectories with small angular momentum that spend most of their time very close to strings, are probably very rapidly dechanneled, which keeps them from accumulating an anomalously large energy loss on passing through the crystal.

Planar transmission. In fig. 12, the intensity distributions around the {111} plane are shown for protons, π^+, and deuterons. For those directions of incidence parallel to the plane, the increase in intensity is approximately a factor of five. The transmission results shown in fig. 12 for the {111} planes are strongly dominated by the finite angular resolution of the detectors (see table 1) which already greatly exceeds ψ_p, as predicted by eq. (2). These predicted angles are indicated in fig. 12. In addition, it is well known that dechanneling is more severe for planar-channeled particles, and this probably also contributes somewhat to the reduced peak-to-nearest background ratio compared to the axis case.

For π^-, no clear planar effects have been found so far.

4.2 Wide-angle scattering experiments

The wide-angle scattering experiments were performed in similar way to the transmission case discussed in sec. 4.1 except that now the criterion for accepting an event is that the scattering angle should be larger than a cut angle β. The value of β should be chosen large enough to ensure the events corresponding to single- rather than to multiple-scattering processes. However, because of the lack of intensity for large values of β, a compromise yielding good statistical accuracy was necessary. Thus a value of $\beta = 3.5$ mrad was used, which is reasonably outside the distribution of the random multiple scattering (see fig. 9) and also much larger than ψ_1.

Figure 13 shows the intensity distribution around the $\langle 110 \rangle$ axis for those protons, π^+, and deuterons in the incident beam which experience a scattering angle larger than 3.5 mrad. For the axis, pronounced dips ($\sim$ 50% of normal yield) in the wide-angle scattering yield are obtained. For the deuterons in general, the effects are less pronounced than they are for π^+ and protons, partly due to the poorer resolution of the detecting system for deuterons. Further, the width of the scan strips (which is the angular distance between data points) is larger for deuterons than for π^+ and protons because of the low beam intensity of deuterons; this larger strip width will also somewhat smear out the dips.

The curves in fig. 13 show dips of about 50% and FWHM near $2\psi_1$. Of course, these effects are affected by our finite angular resolution. Because we have no depth resolution, the results also represent the scattering yield averaged over the depth of the sample.

4.3. Attempt to do blocking experiment

Normally blocking experiments are accomplished by placing the crystal axis far from the incident-beam direction and by looking at wide-angle scat-

tering into dire ctions near the axis direction (see fig. 3c). This procedure is, however, not satisfactory to us because the yield of very wide-angle scattering particles is extremely low. Therefore, in order to get sufficient intensity, we were restricted to use scattering angles down to 1.5 mR. Hence the data were obtained with the axis direction still oriented along the average incident-beam direction, and the method of analysis described below was used.

Figure 15 shows schematically the method we have used in our attempt to isolate the blocking effect. Each incident-beam direction not leading to channeled motion will have an angular distribution on the back side of the crystal consisting of a broad Gaussian multiple-scattering part with a dip at the exit angle along the axis direction. Such a distribution for the component of the beam at incidence angle θ_i is sketched in the figure (fig. 15a).

Data were disregarded by eliminating all events from the incident-beam particles to one side of a dividing line in the incident, two-dimensional angle space (see fig. 15b). The dividing line and the center of the crystal define a "cut plane", which was placed 1.5 mrad away from the axis direction (see fig. 15a). Only incident particles on the side of the plane not containing the axial direction are accepted, and incident axial channeling is thus eliminated. The dips shown in fig. 16 were then obtained by scanning parallel to the dividing line through the axis direction (see fig. 15c) for the exiting particles. The data in fig. 16 are presented unnormalized,

Figure 16 shows the unnormalized angular distributions obtained for protons and π^+ with momentum 1.15 GeV/c transmitted through a 1-mm thick germanium crystal. Dips of nearly 50% are obtained. As the scattering angles are small, we refrain from a comparison with theoretical calculations.

4.4. Energy-loss experiments

While some of our energy-loss results have been presented recently in a brief note[2], we present below a more complete set of data that now includes results for planar-channeled particles and axial-channeled π^-. A detailed theoretical analysis then follows.

The germanium-detector pulse-height spectra for 1.35 GeV/c protons and π^+ and for 1.35 GeV/c π^- are shown in figs. 17-20. In the figures, the pulse height has been converted into energy deposited in the depletion layer from a calibration obtained by exposing the detector to gamma rays from ^{57}Co and ^{137}Cs sources.

The open circles correspond to energy-loss spectra of particles belonging to the random beam; only particles for which angles in incidence lie far away from any major axis or plane are selected. The filled circles show the energy-loss spectra obtained for particles with incident angles to the $\langle 110 \rangle$ axis aligned within 0.9 mrad and with scattering angles of less than 0.35 mrad. These angular constraints ensured that the energy spectra mainly contains contributions from channeled particles.

It is clearly seen that for channeled protons and π^+, the energy-loss is reduced considerably, as compared to the random beam. For π^- (fig. 19). the energy-loss spectra for channeled and random beams are nearly the same.

Figure 20 shows similar results obtained for the {111} plane. Also here, a very pronounced reduction in energy loss for channeled particles is observed. The width of the energy-loss distribution for the planar-channeled particles is reduced to around 15 keV, which is roughly the energy resolution of the detector.

Under E_{det}, table 2 contains the measured mean energy deposited in the detector for protons, π^+, and π^- for a random-incidence direction. Under $E_{leading\ edge}$, the characteristic energy loss associated with the leading edge of the channeled energy-loss spectrum for protons and π^+ can be found.

Finally, fig. 21 shows an angular map of all π^+ in the incident beam that have deposited only half of the random energy loss in the detector. The ⟨110⟩ axis and the {110} and {111} planes are clearly visible. Using two crystal detectors turned around the axial direction relative to each other to eliminate planar effects along a crystal plane, one can easily produce well-collimated point or line beams in angle space. From the curves shown in fig. 10, it appears that the transmitted beam consists of two parts: A peak characterized by the critical angle ψ_1 and an almost constant background. The use of two crystals in order to eliminate planar effects yields at the same time a reduction of the background. The beam quality after passage through the crystals may be characterized by the emittance $\varepsilon \simeq A\,\psi_1^2$, where A is the useful area of the crystals. In this actual case, the emittance is 10-15 mm^2 $(mrad)^2$. It is notable that a crystal-collimator does not behave like a set of diaphragms, where the beam optics is determined by geometry. For instance the opening of diaphragms influences the angular distribution while for a crystal-collimator, the angular distribution of the exiting particles is not affected by the area A of the crystals.

Before any comments are made about the energy-loss results for channeled particles, it would seem reasonable that the somewhat better understood stopping theory for random penetration be applied to our experimental results for nonaligned directions of incidence. Here it is essential to realize that the energy loss of the particle in passing through the germanium-crystal detector does not correspond exactly to the energy deposited in the sample, as measured by the total number of electron pairs created. This is due to the fact that it is possible for energetic recoil electrons associated with the energy-loss process to completely escape from the detector. For example, a close collision between a penetrating 1.35 GeV/c π^+ and an electron results in 90-MeV recoil electrons . For our detector geometry, on the average, recoil electrons with energies in excess of 400 keV escape from the germanium crystal without creating the appropriate number of hole electron pairs characteristic of that portion of the energy-loss process. Thus, the energy deposited in the detector is not the energy loss experienced by the particle. Nevertheless, these quantities are closely related. A simple formula for the average energy-loss rate restricted to energy transfers smaller than T_o is given by Fano[15] as

$$-\frac{dE}{dx_{rest}} = \frac{2\pi e^4 Z_2 N}{m_e v^2}\left\{2\ell n\frac{2m_e v^2\gamma^2}{I} - 2\frac{v^2}{c^2} + \left[\ell n\frac{T_o}{2m_e v^2\gamma^2} - \frac{T_o}{2m_e c^2\gamma^2} + \frac{v^2}{c^2}\right]\right\}, \quad (7)$$

where the term in square brackets represents a modification of the normal energy deposited due to a lack of contribution from energy transfers greater than T_o . The mean energy loss for the case of random penetration is given by eq. (7) with

$$T_o = 2m_e v^2\gamma^2 \quad , \quad (8)$$

which is the maximum energy transfer in a 'head-on' collision. In the above two formulas, v and c are the velocities of the incident particle and light,

respectively, m_e is the electron rest mass, and γ is the relativistic factor $(1 - v^2/c^2)^{-1/2}$. I is Bethe's well-known mean-excitation energy of target atoms. Apart from some algebraic manipulations, eq. (7) corresponds to eq. (88) in ref. [19] without contribution from shell effects or Cerenkov radiation loss.

Table 2 gives the theoretical mean-energy loss ΔE_{rand} for the random beam. The value for protons is simply determined by eqs. (7) and (8) and the germanium-crystal thickness. For pions, the density effect is expected to be important at this energy. A reduction by 5% from the value predicted by eqs. (7) and (8) has been assumed[20]. ΔE_{detec} indicates the experimentally determined mean energy deposited in the detector by the random beam. ΔE_{rest} is the restricted energy loss from eq. (7) with a value T_o = 400 keV assumed for both protons and pions with the density-effect correction for pions included.

The value of T_o was arrived at in the following way. The recoil electron energy vs. recoil-angle kinematics was determined. With the help of electron-range energy tables[20], the angle at which electrons would escape the crystal was determined for different depths. The recoil energy corresponding to these angles was then averaged over the depth of the crystal to obtain an average T_o. While a more detailed program for calculating T_o may be envisaged, taking into account multiple scattering and energy loss of the escaping electrons, the difficulty of such a calculation, coupled with the insensitivity of eq. (7) to the result, has let us feel content with the estimate of T_o described above.

The agreement between E_{detec} and E_{rest} is quite good and suggests that the random energy-loss part of the experiment gives reasonable results. Experimental errors in the values for ΔE_{detec} are of the order of 1%. We

have also obtained qualitative, though not totally quantitative, agreement with the Landau-Vavilov energy-loss straggling distributions for the random beam. Due to the difference between $T_o = 400$ keV and $2m_e v^2\gamma^2$, this is not very surprising.

We now turn to the more important aspect of our experiment, the channeling energy-loss results. Recently, Golovchenko and Esbensen[21] have presented a theory for stopping power for channeled particles, which results in the following simple analytical formula for the transverse position-dependent stopping in the limit of high velocities, ($v\gamma > Z_2 v_o$; $v_o = e^2/\hbar$). Their result is:

$$-\frac{dE}{dx} = \frac{4\pi Z_1^2 e^4}{m_e v^2} N\left\{ Z_2 \ell n \frac{2m_e v^2}{I} + \Sigma_{\bar{G}\neq\bar{0}} e^{i\bar{G}\cdot\bar{b}} \rho(G) \ell n \frac{2m_e v}{\hbar G} \right\} , \qquad (9)$$

where $\bar{G}$'s are reciprocal lattice vectors in the transverse space, $\bar{b}$ is the position of the penetrating particle in the transverse space, and ρ is the Fourier transform of the electronic-charge density in the crystal.

The above result did not include retardation effects and is not strictly proper for stopping in the relativistic region. This effect may easily be remedied by noting that the relativistic contribution from transverse excitations (resulting from the vector-potential part of the electron-particle interaction) satisfied a strict equipartion in the random case with equal contributions coming from very low and very high momentum transfers. Thus a density-dependent close-collision part of the random component may be added to formula (9) along with the random, path-independent, distant-collision (i.e., low-momentum transfer) part. The result is

$$-\frac{dE}{dx} = \frac{4\pi Z_1^2 e^4}{m_e v^2} N\left\{ Z_2 \ell n \frac{2m_e v^2\gamma^2}{I} - \frac{v^2}{c^2} + \right.$$
$$\left. + \Sigma_{\bar{G}\neq\bar{0}} e^{i\bar{G}\cdot\bar{b}} \rho(G) \left\{ \ell n\left(\frac{2m_e v\gamma}{\hbar G}\right) - \frac{v^2}{2c^2} \right\} \right\} , \qquad (10)$$

which depends only on Bethe's I value and the electronic-charge density as properties of the medium.

Equation (10) has been calculated using Fourier components of the electronic-charge density given by Doyle and Turner[22]. The results for 1.35 GeV/c protons in the ⟨110⟩ germanium are shown in fig. 22. From this figure it is seen that the minimum average energy-loss rate is 240 keV/mm for particles travelling directly in the middle of the channel. Part of the reason for this reduction is the very low electron density along that particular path in the crystal. That is, for these particles, the energy-loss contribution associated with close collisions is greatly suppressed. This has two important consequences. First, corrections for escape of high-energy recoil electrons are much less important for proper channeled particles than for random ones. Second, fluctuations in energy loss, which are mainly associated with fluctuations in the number of close collisions, will also be strongly reduced for proper channeled particles than for random ones. We therefore feel reasonably confident in associating the low-energy edge of the experimental, channeled energy-loss distributions with the best channeled low energy-loss results shown in figs. 17 and 18. These values are contained in table 2 for protons and π^+. For π^+, the random density effect has been included. The agreement between theory and experiment is quite satisfactory and should improve when dechanneling effects are minimized by making the experiment on thinner samples. We also notice that Dettmann's prediction[23] of the ratio of channeled and random stopping power in the limit of high velocities does not agree with the results in table II.

The problem of calculating the entire distribution of losses is a very complex one indeed. There will be a distribution of $\bar{b}$ values (eqs. (9) and

(10)) associated with all channeling trajectories, and for each $\bar{b}$ value, particularly for those associated with large transverse energies, there will be a broad distribution of losses associated with energy-loss straggling. In addition, there will be the problem of recoil-electron escape for large transverse-energy trajectories. The reader will perhaps be sympathetic with our decision to limit this analysis to the best channeled particles.

The general significance of the π^- energy-loss results have already been mentioned in connection with the π^- transmission experiments (sec. 4.1). We hope to report on energy-loss calculations for the bound trajectories, based upon eq. (10) and upon statistical estimates of transverse spatial distributions for such states.

5. Concluding Remarks

From the data and analysis presented, several conclusions may be drawn. Thus, channeling conditions may be established and maintained for both positive and negative particles through macroscopic distances (i.e., ~1 mm) in nearly perfect crystals.

Although the angles associated with the effect are small (~1 mrad) for particles at energies around 1 GeV, channeling effects become increasingly important at higher energies in the sense that critical angles decrease only as $(pv)^{-1/2}$, while multiple-scattering angles associated with random penetration through detectors, windows, and related material decrease as $(pv)^{-1}$. Experiments are, in fact, now being performed at beam moments $\sim$ 15 GeV/c to take advantage of this prediction, which should greatly improve the angular resolution of the measurements relative to the angles in question.

Strong channeling energy-loss effects also persist at very high ener-

gies, thus making the behaviour of positive, channeled particles detectable even when compared with broad Landau-Vavilov distributions normally encountered in energy-loss experiments. Small crystals (energy-loss detectors capable of (i) collimating positive high-energy particles and (ii) discriminating between positive and negative particles, result.

Finally, the successful observation of phenomena at high-energy physics accelerators, where new particles and reactions are accessible, naturally leads us to consider more seriously the extension of certain applications with which we are familiar at lower energies. In particular the blocking technique has already allowed direct measurement of the lifetime of compound nuclei in the 10^{-16}-10^{-18} sec region[24]. Detailed investigations of suitable elementary-particle cases are currently being performed.

6. Acknowledgments

The authors are grateful to J.U. Andersen, J. Lindhard, and H.E. Schiøtt for fruitful discussions. We are indebted to O. Alstrup and L. Andersen of the Technical University, Lyngby, for germanium-crystal preparation and testing. We should also like to thank S. Olesen for his help with the construction of target and goniometer arrangements. The beam tube and goniometer were manufactured at the Niels Bohr Institute, Copenhagen, and for this we are grateful to K. Gudbjerg Hansen. The authors especially express their gratitude to the Département d'Instrumentation et Techniques Nucléaires, Strasbourg, for the construction and manufacturing of the crystal-cooling system and germanium detectors. The help of P. Siffert and R. Stuck has been of particularly vital importance. The support from the Danish Committee for Accelerator Physics, which made Danish participation in the collaboration possible, is also gratefully acknowledged.

References

1) O. Fich, J.A. Golovchenko, K.O. Nielsen, E. Uggerhøj, G. Charpak, and F. Sauli, Phys. Letters 57B (1975) 90

2) O. Fich, J.A. Golovchenko, K.O. Nielsen, E. Uggerhøj, C. Vraast-Thomsen, G. Charpak, S. Majewski, and F. Sauli, Phys. Rev. Letters 36 (1976) 1245

3) D. Allen, D. Gockley, G. Lazo, W. Gibson, H. Wegner, and A. Kanotsky, Lett. Nuovo Cimento 15 (1976) 529

4) D.S. Gemmell, Rev. Mod. Phys. 46 (1973) 129

5) J. Lindhard, Kgl. Danske Videnskab. Selskab, Mat.-Fys. Medd. 34 (1965) No. 14

6) J.U. Andersen, W.M. Augustyniak, and E. Uggerhøj, Phys. Rev. B 3 (1971) 705

7) E. Uggerhøj, Phys. Letters 22 (1966) 382 and E. Uggerhøj and J.U. Andersen, Can. J. Phys. 46 (1968) 543

8) Ph. Lervig, J. Lindhard, and V. Nielsen, Nucl. Phys. A 96 (1967) 481

9) S.T. Picraux and J.U. Andersen, Phys. Rev. 186 (1969) 267

10) N. Bohr, Kgl. Danske Videnskab. Selskab, Mat.-Fys. Medd. 18 (1948) No. 8

11) E. Bøgh and J.L. Whitton, Phys. Rev. Letters 19 (1967) 533

12) S. Kjær Andersen, F. Bell, F. Frandsen, and E. Uggerhøj, Phys. Rev. B 8 (1973) 4913

13) H. Kumm, F. Bell, R. Sizmann, H.J. Kreiner, and D. Harder, Rad. Effects 12 (1972) 53

14) A. Ya. Bobudaev, V.V. Kaplin, and S.A. Vorobiev, Phys. Letters 45A (1973) 71

15) J.U. Andersen, S. Kjær Andersen, and W.M. Augustyniak, Kgl. Danske Videnskab. Selskab, Mat.-Fys. Medd., to be published

16) A. Breskin, G. Charpak, F. Sauli, M. Atkinson, and G. Schultz, Nucl. Instr. Methods 124 (1975) 189

17) H. Herzer, S. Kalbitzer, J.P. Ponpon, R. Stuck, and P. Siffert, Nucl. Instr. Methods 101 (1972) 31

18) E. Bonderup, H. Esbensen, J.U. Andersen, and H.E. Schiøtt, Rad. Effects 12 (1972) 261 and H.E. Schiøtt, E. Bonderup, J.U. Andersen, H. Esbensen, M.J. Pedersen, D.J. Elliott, and E. Lægsgaard, in Proc. 5th Int. Conf. on Atomic Collisions in Solids, Gatlinburg, Tenn., (1973) Vol. 2, p. 843

19) U. Fano, Ann. Rev. Nucl. Sci. 13 (1963) 67

20) Studies in Penetration of Charged Particles in Matter. Nat. Acad. Sci.-National Research Council, Publ. 1133

21) J.A. Golovchenko and H. Esbensen, to be published

22) P.A. Doyle and P.S. Turner, Acta Cryst. A24 (1968) 390

23) K. Dettmann, Z. Physik A 272 (1975) 227

24) W. Gibson, Ann. Rev. Nucl. Sci. 25 (1975) 465

Figure Captions

Fig.1 a) Longitudinal view. Collision of a positive particle with a single string of atoms. Particles with $\theta_i \leq \psi_1$ - trajectory 1 - belong to the aligned beam. The minimum distance of approach is given by: $E_\perp = \frac{1}{2} pv\theta_i^2 = U(r_{min})$. Particles with $\theta_i > \psi_i$ - trajectory 2 and 3 - belong to the random beam. b) Transverse view. The string direction is perpendicular to the plane.

Fig.2 Motion in transverse plane perpendicular to the ⟨110⟩ direction in Ge. The average atomic potential is shown as equipotential contours labelled 7 , 11 , 23 , 34 , and 126 eV. The contours are also labelled by the value for the incident angle θ_i giving the transverse energy $E_\perp = 1/2\, p\, v\, \theta_i^2$ required for a 1.35 GeV/c π^+ to penetrate into the contour in question. The channeled particles - trajectory 1 and 2 - will normally wander among adjacent "pipes" formed by the string of atoms.

Fig.3 Schematic arrangement of three typical channeling experiments. a) Transmission experiment. b) Wide-angle experiments. c) Blocking experiment.

Fig.4 Experimental layout.

Fig.5 Schematic drift-chamber geometry.

Fig.6 Drift chamber with screening electrodes, drift wires, and field wires, from Ref. 16.

Fig.7 Schematic diagram of the on-line electronic data-ecquisition system.

Fig.8 Stereogram showing intensity distribution of 1.15 GeV/c π^+ after transmission through a 1 mm thick Ge crystal. Only π^+ that have been scattered less than 0.35 mrad are registered. The axial distribution is obtained by choosing a narrow strip

through the axis, dashed line. The planar distribution is measured by integrating in strips parallel to the plan. The framed region is such a scan area.

Fig.9 Random multiple scattering of 1.35 GeV/c π^+ into a 0.67 mm thick Ge crystal.

Fig.10 Intensity distribution of transmitted 1.15 GeV/c π^+, protons, and deuterons as a function of the angle between the $\langle 110 \rangle$ axis and the exit direction. The overall scattering angle is less than 0.35 mrad. Crystal thickness 1 mm and temperature around 300 K.

Fig.11 Intensity distribution of transmitted 1.15 GeV/c π^- under the same condition as described in Fig.10.

Fig.12 Intensity distribution of transmitted 1.15 GeV/c π^+, protons, and deuterons as a function of angle between the $\{111\}$ plane and the exit direction. The overall scattering angle is less than 0.35 mrad. Crystal thickness 1 mm and temperature around 300 K. Calculated critical angles ψ_p are indicated.

Fig.13 Intensity distribution of wide-angle scattering yield for 1.15 GeV/c π^+, protons, and deuterons as a function of angle between incident direction and the $\langle 110 \rangle$ axis. The overall scattering angle is larger than 3.5 mrad. Crystal thickness 1 mm and temperature around 300 K.

Fig.14 Calculated wide-angle scattering yields for 1.15 GeV/c protons in the $\langle 110 \rangle$ axial direction of Ge at room temperature as a function of incident angle θ_i in units of ψ_1 = 0.72 mrad. The yields are averaged over crystal thickness R = 0.24 , 0.48 , 0.72 , 0.96 , and 1.29 mm.

Fig. 15: Schematic arrangement showing the principle of measuring the blocking dip.

Fig. 16: Blocking dips for 1.15 GeV/c π^+ and protons transmitted through a 1-mm Ge crystal.

Fig. 17: Pulse-height spectra from a Ge detector for 1.35 GeV/c protons. • Spectrum from particles within 0.9 mrad of ⟨110⟩ axis direction; o spectrum from incident angles, not including any major axial or planar direction. Scattering angle smaller than 0.35 mrad. Crystal thickness 0.67 mm.

Fig. 18: Pulse-height spectra from a Ge detector for 1.35 GeV/c π^+. • Spectrum from particles within 0.9 mrad of ⟨110⟩ axis direction; o spectrum from incident angles, not including any major axial or planar directions. Scattering angle smaller than 0.35 mrad. Crystal thickness 0.67 mm.

Fig. 19: Pulse-height spectra from a Ge detector for 1.35 GeV/c π^-. • Spectrum from particles within 0.9 mrad of ⟨110⟩ axis direction; o spectrum from incident angles, not including any major axial or planar direction. Scattering angle smaller than 0.5 mrad. Crystal thickness 0.67 mm.

Fig. 20: Pulse-height spectra from a Ge detector for 1.35 GeV π^+. • Spectrum from particles within 0.9 mrad of {111} planar direction and scattering angle smaller than 0.5 mrad. Crystal thickness 0.67 mm.

Fig. 21: Stereogram showing intensity distribution of incident π^+ that have lost less than 260 keV in energy by going through the 0.67 mm thick Ge crystal. Original energy 1.35 GeV/c. Compare with fig. 8.

Fig. 22: Contours of equal stopping for 1.35 GeV/c protons in the transverse plane of the ⟨110⟩ axial direction in Ge.

Table I

Contributions of the drift-chamber accuracy $\Delta\theta_{DC}$ and of multiple Coulomb scattering $\Delta\theta_{MS}$ to the overall instrument angular resolution $\Delta\theta$ on the exiting tracks at 1.35 GeV/c. All angles are in mrad and represent FWHM of the distributions.

	$\Delta\theta_{DC}$	$\Delta\theta_{MS}$	$\Delta\theta$
Pions	0.14	0.17	0.22
Protons	0.14	0.19	0.25
Deuterons	0.14	0.28	0.32

Table II

Particle	ΔE_{rand} a)	ΔE_{rest} b)	ΔE_{det} c)	$\Delta E^{(exp)}_{lead.edge}$	$\Delta E^{(theory)}_{lead.edge}$ e)
Protons	579	539	538	~180 keV	169
π^+	537	423	421	~180 keV	158
π^-	537	423	424	-	-

a) Theoretical random energy-loss with density effect included for pions.

b) Theoretical restricted energy-loss with T_o = 400 keV and density effect included for pions.

c) Experimental mean energy deposited in detector.

d) Leading edge of channeled energy-loss distributions; experiment.

e) Leading edge of channeled energy-loss distributions; theory.

SINGLE STRING COLLISION

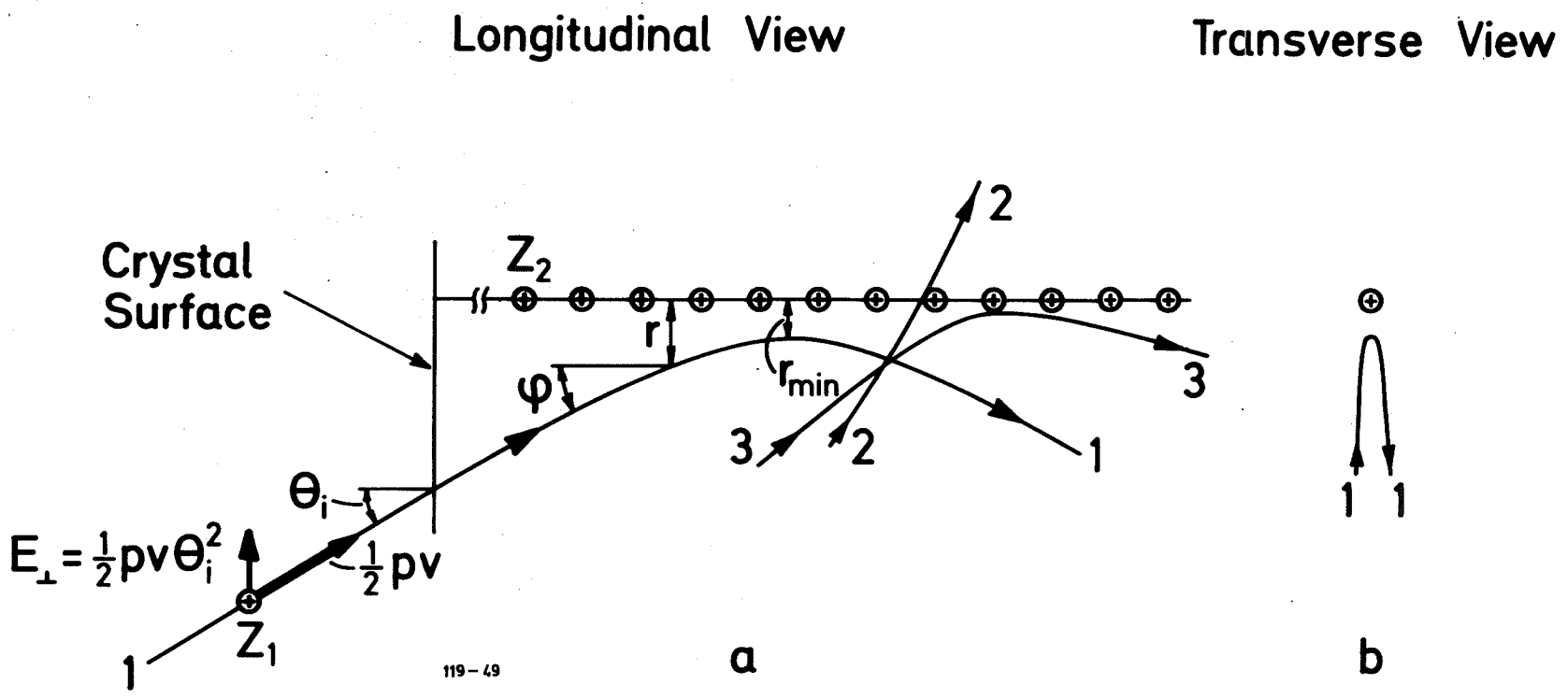

Fig. 1

MOTION IN TRANSVERSE PLANE

$$E_{\perp} = \tfrac{1}{2} pv\theta_i^2 = \tfrac{1}{2} pv\varphi^2 + U(r)$$

1.35 GeV/c π^+ in a Germanium Crystal

1 : θ_i = 0.18 mrad 2 : θ_i = 0.4 mrad 3 : $\theta_i > \psi_1$ = 0.59 mrad

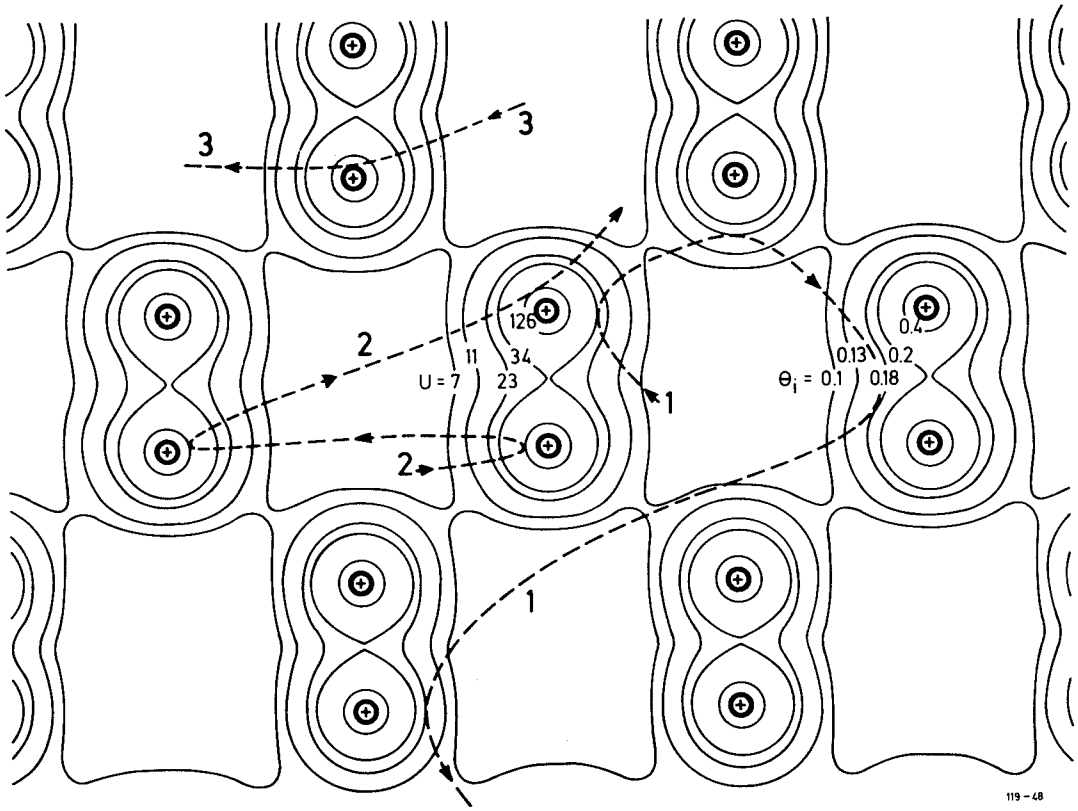

Fig. 2

EXPERIMENTAL GEOMETRIES

Transmission Experiment

119 – 42A

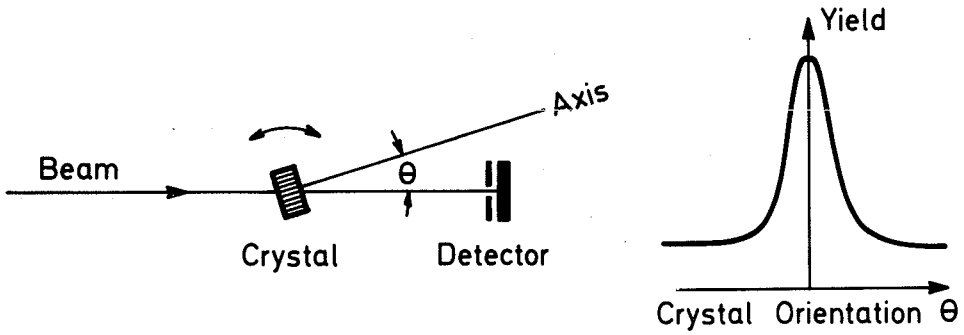

a

Wide – Angle Scattering

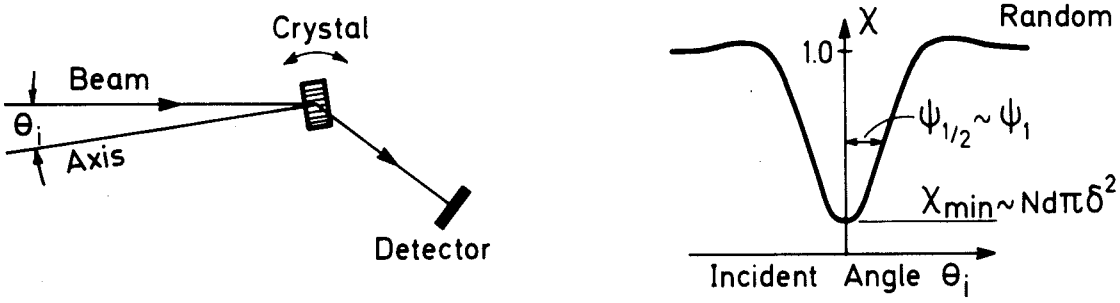

b

Blocking

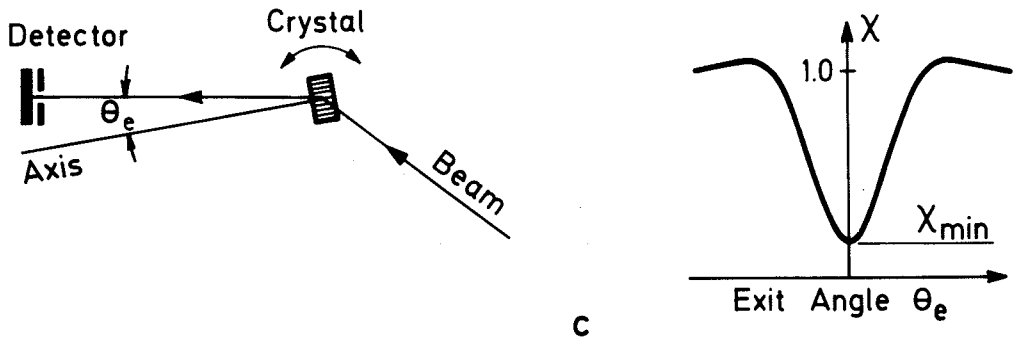

c

Fig. 3

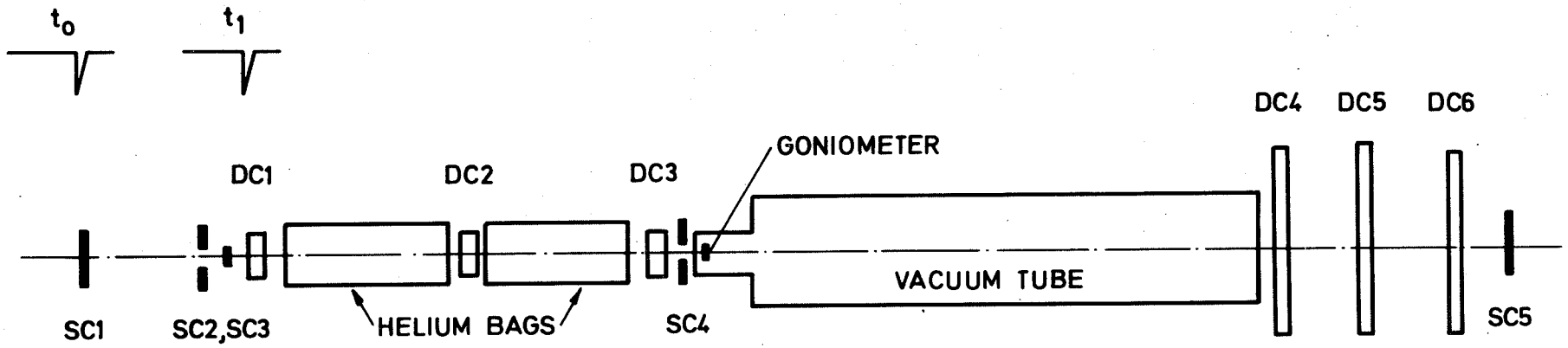
t_o
t_1
DC1
DC2
DC3
GONIOMETER
DC4
DC5
DC6
VACUUM TUBE
SC1
SC2,SC3
HELIUM BAGS
SC4
SC5

Fig. 4

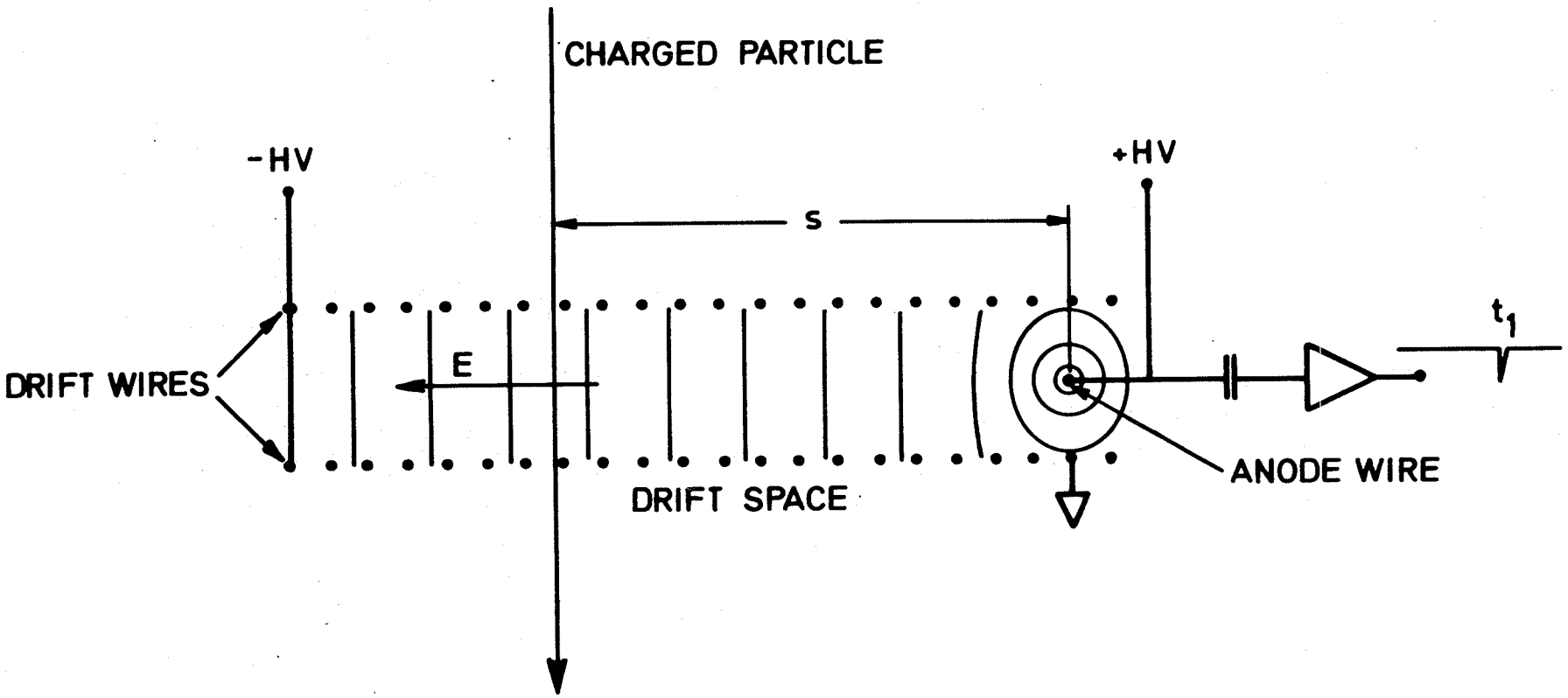
CHARGED PARTICLE
-HV
+HV
s
DRIFT WIRES
E
t_1
DRIFT SPACE
ANODE WIRE

Fig. 5

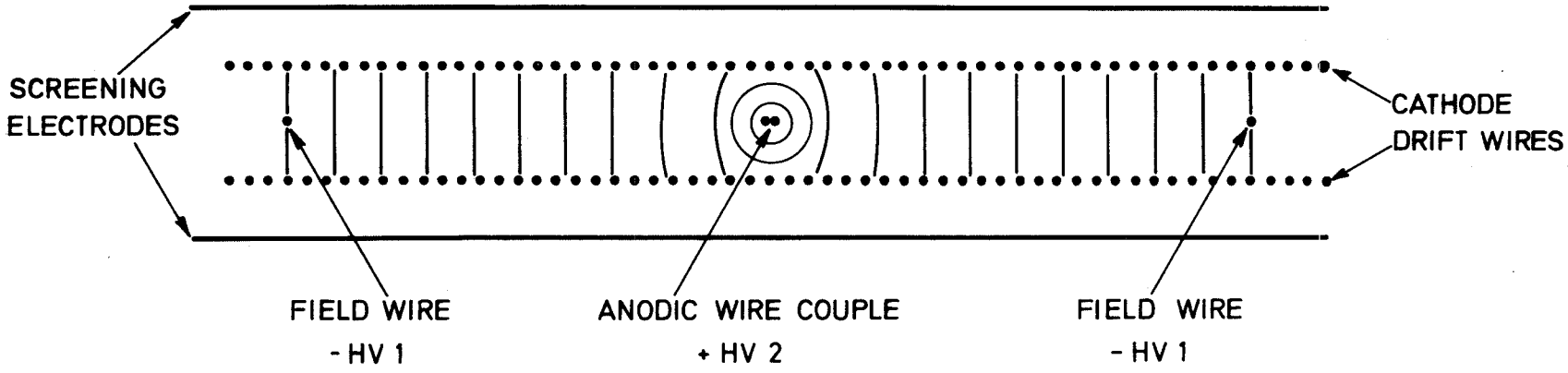
SCREENING
ELECTRODES
CATHODE
DRIFT WIRES
FIELD WIRE
- HV 1
ANODIC WIRE COUPLE
+ HV 2
FIELD WIRE
- HV 1

Fig. 6

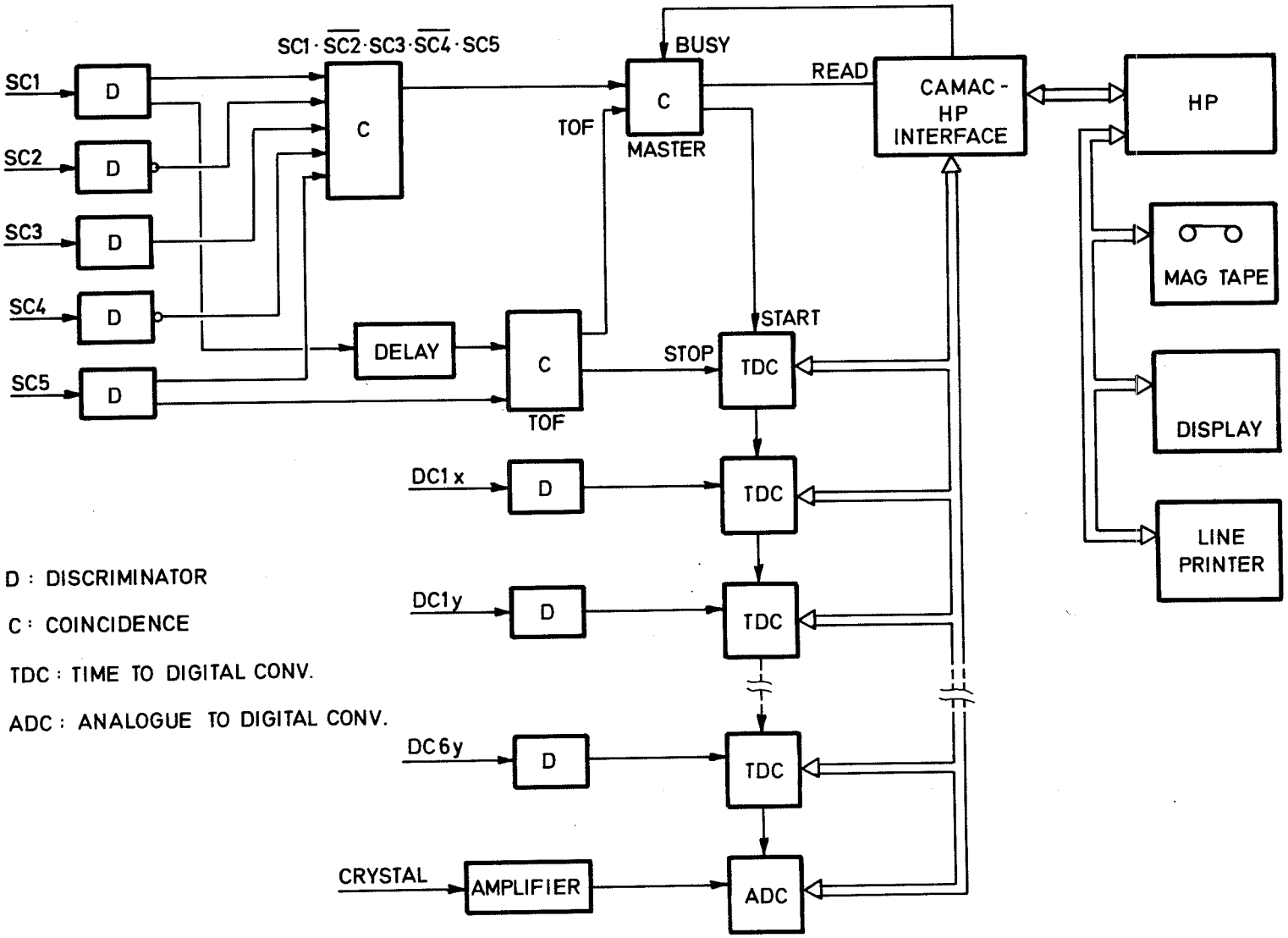
SC1 · SC2 · SC3 · SC4 · SC5
BUSY
READ
CAMAC - HP INTERFACE
HP
MAG TAPE
DISPLAY
LINE PRINTER
SC1
SC2
SC3
SC4
SC5
D
C
TOF
MASTER
DELAY
START
STOP
TDC
DC1 x
DC1 y
DC6 y
CRYSTAL
AMPLIFIER
ADC
D : DISCRIMINATOR
C : COINCIDENCE
TDC : TIME TO DIGITAL CONV.
ADC : ANALOGUE TO DIGITAL CONV.

Fig. 7

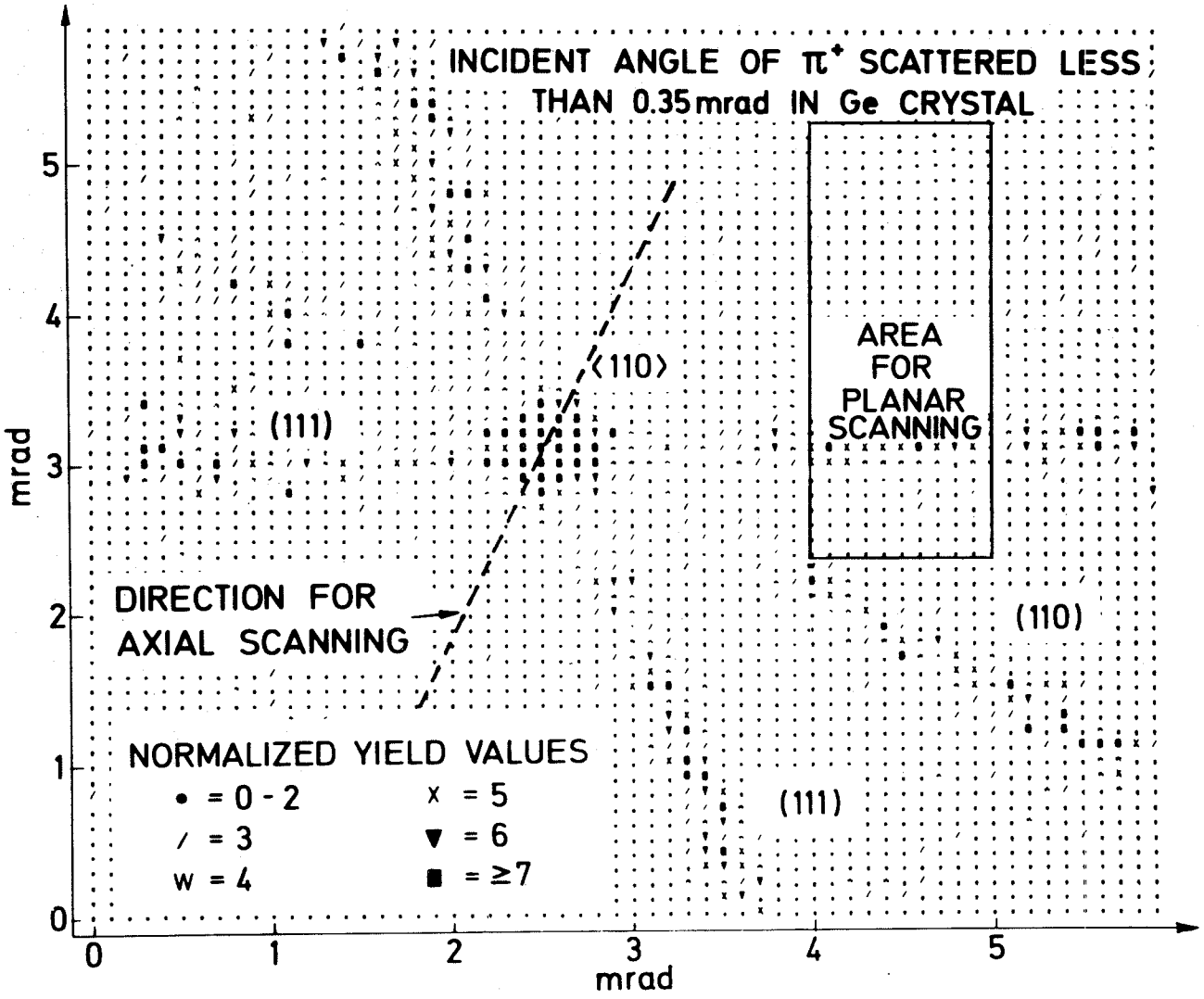
INCIDENT ANGLE OF π⁺ SCATTERED LESS THAN 0.35 mrad IN Ge CRYSTAL
AREA FOR PLANAR SCANNING
⟨110⟩
(111)
(110)
(111)
DIRECTION FOR AXIAL SCANNING
NORMALIZED YIELD VALUES
• = 0 - 2
/ = 3
w = 4
x = 5
▼ = 6
■ = ≥7
mrad
mrad
0
1
2
3
4
5

Fig. 8

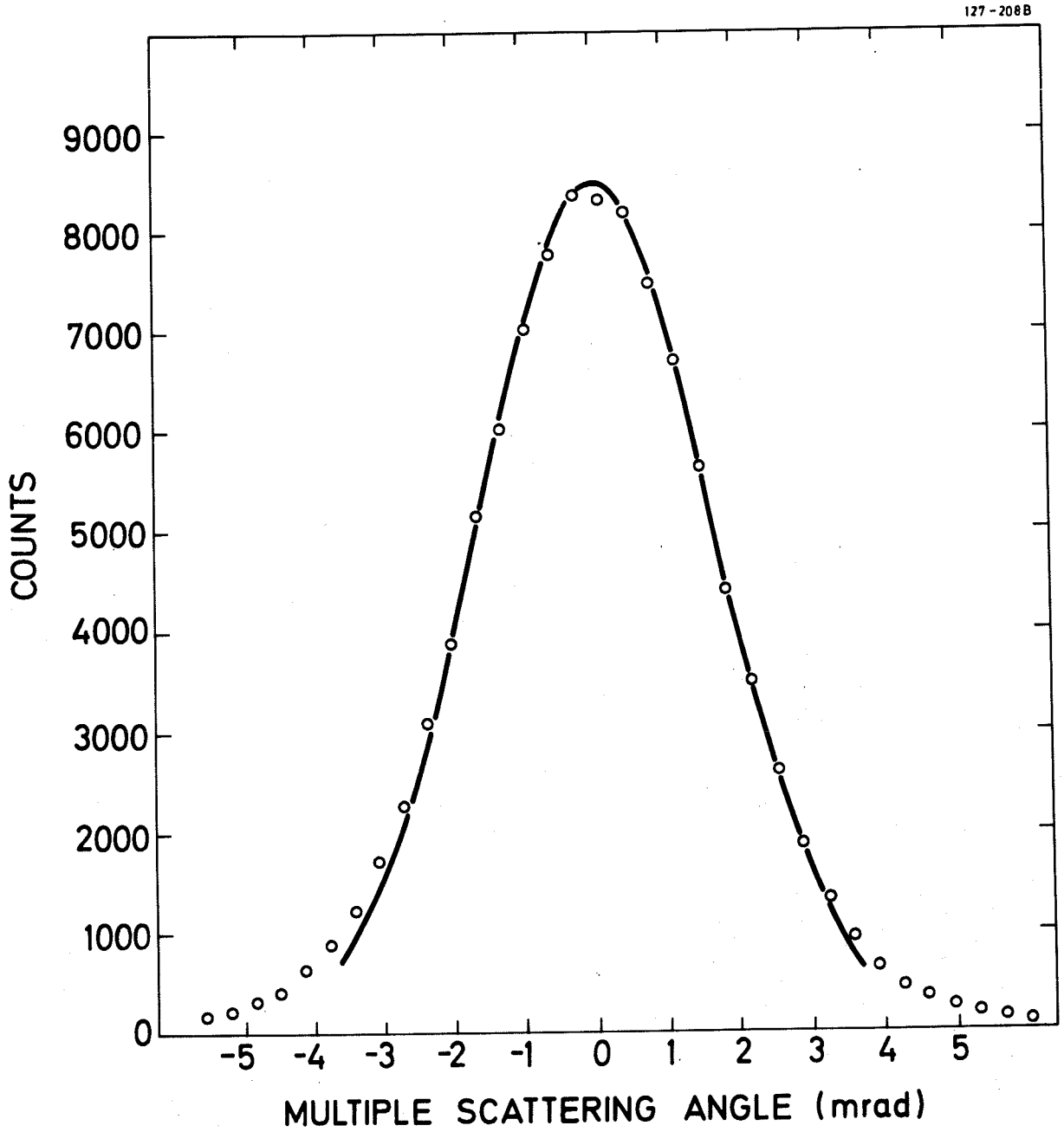
127-208B
COUNTS
9000
8000
7000
6000
5000
4000
3000
2000
1000
0
-5
-4
-3
-2
-1
0
1
2
3
4
5
MULTIPLE SCATTERING ANGLE (mrad)

Fig. 9

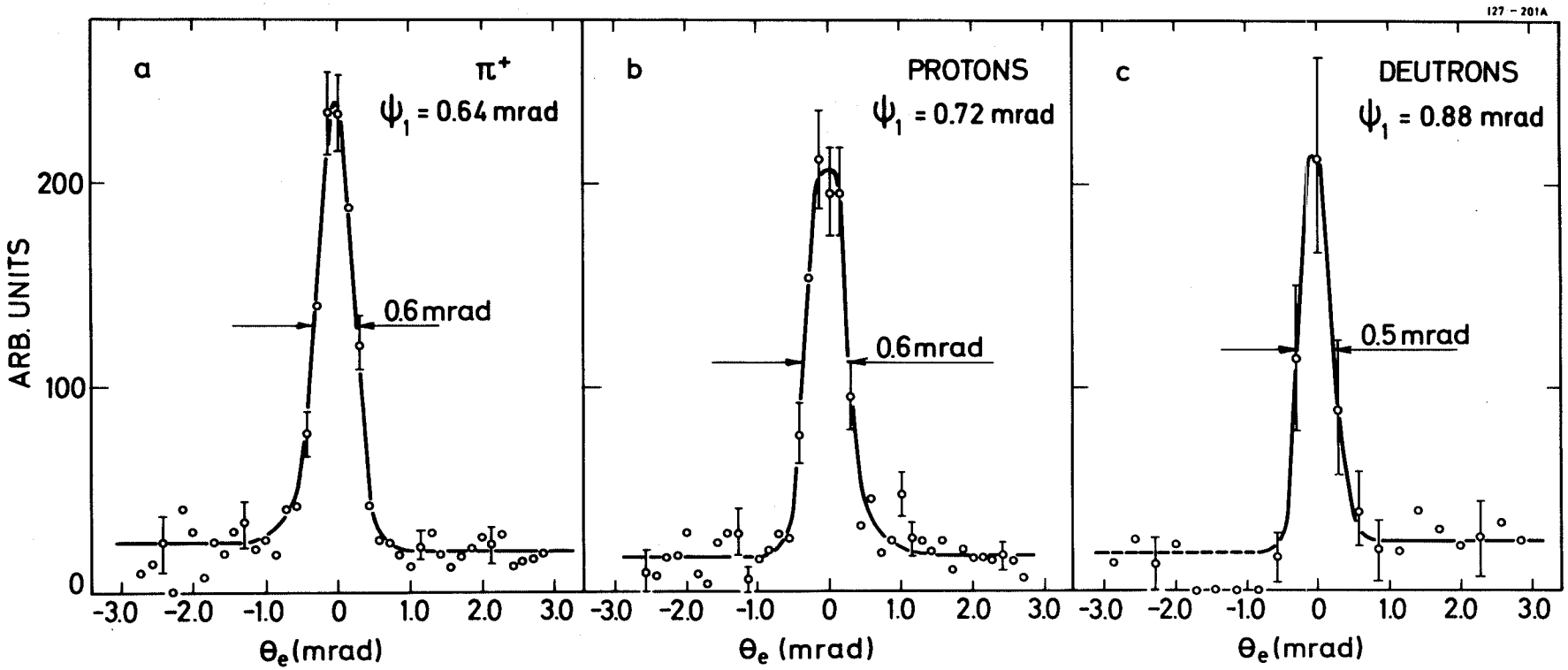
127 - 201A
a
π+
ψ1 = 0.64 mrad
0.6 mrad
b
PROTONS
ψ1 = 0.72 mrad
0.6 mrad
c
DEUTRONS
ψ1 = 0.88 mrad
0.5 mrad
ARB. UNITS
200
100
0
-3.0 -2.0 -1.0 0 1.0 2.0 3.0
θe (mrad)

Fig. 1o

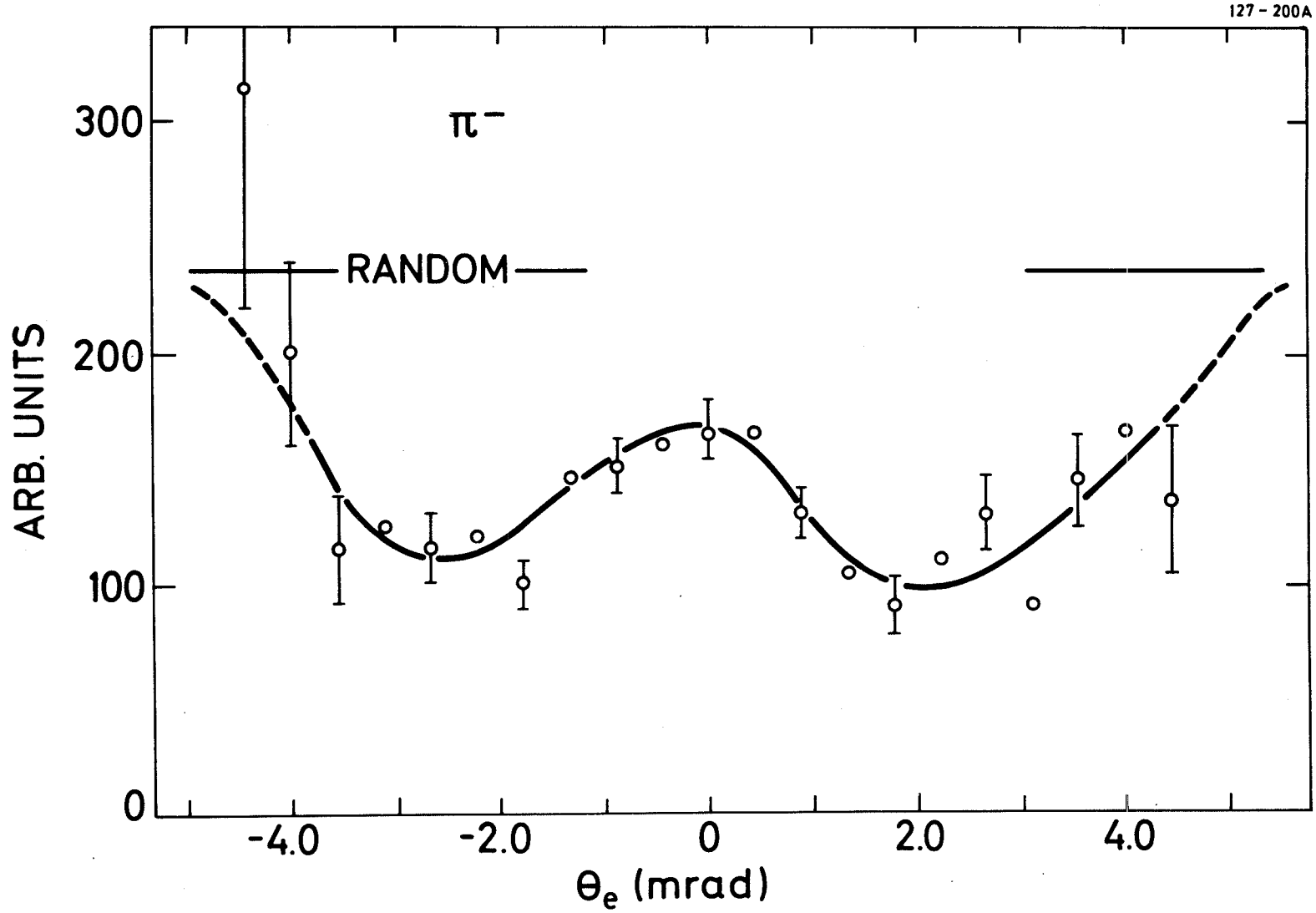

Fig. 11

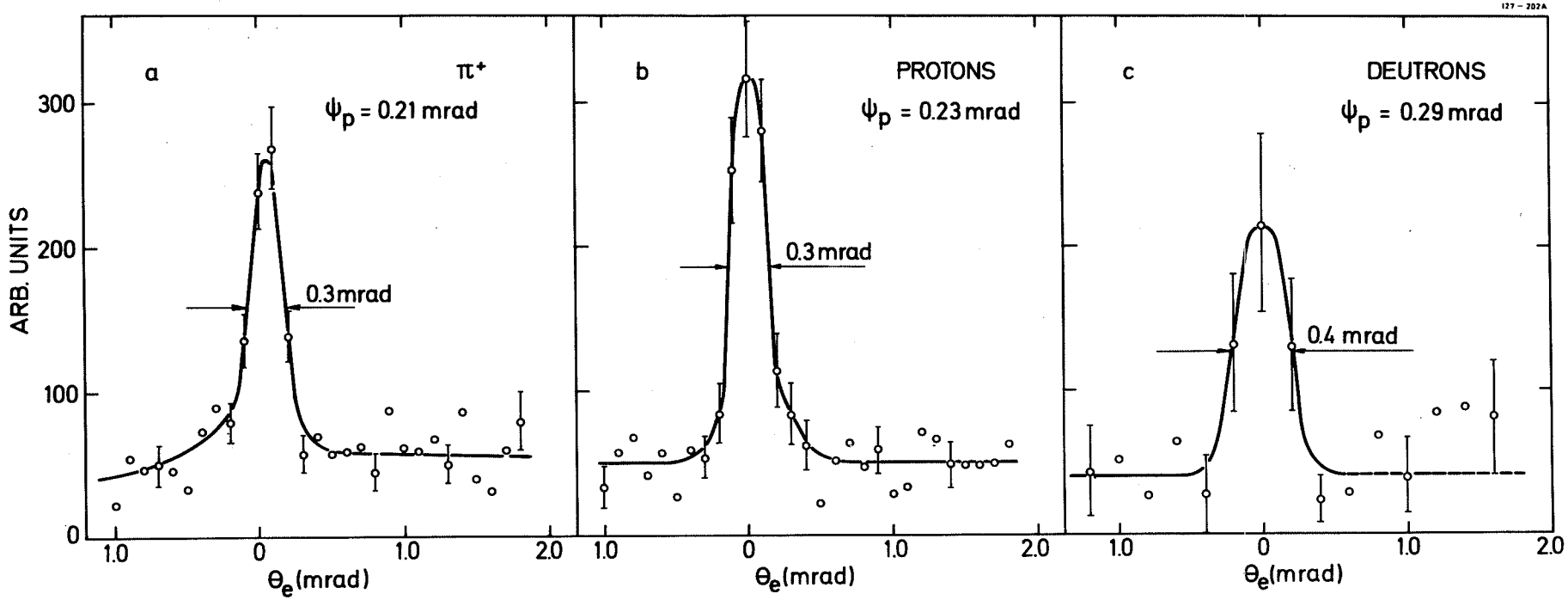
127 – 202A
a
π+
ψp = 0.21 mrad
0.3 mrad
b
PROTONS
ψp = 0.23 mrad
0.3 mrad
c
DEUTRONS
ψp = 0.29 mrad
0.4 mrad
ARB. UNITS
300
200
100
0
1.0
0
1.0
2.0
θe (mrad)

Fig. 12

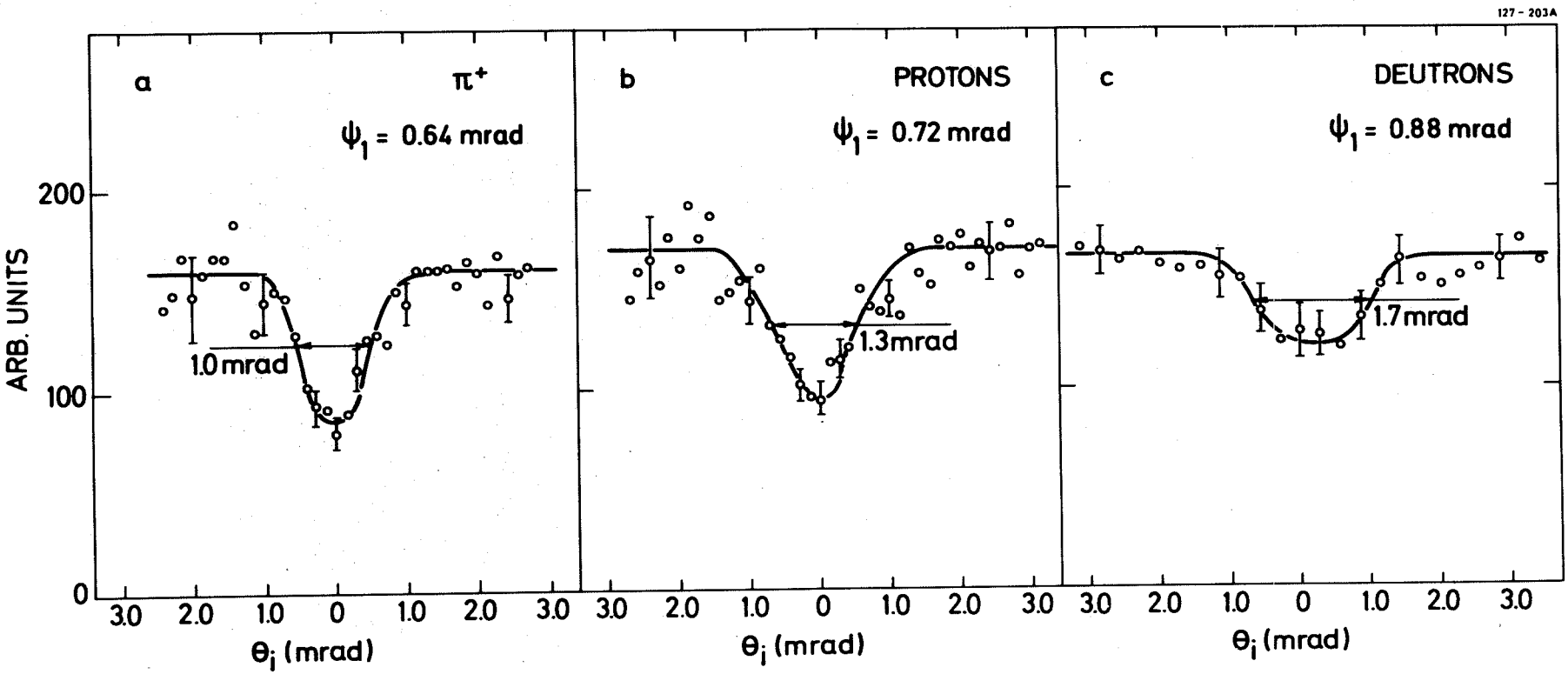
127 - 203A
a
π+
ψ1 = 0.64 mrad
1.0 mrad
b
PROTONS
ψ1 = 0.72 mrad
1.3 mrad
c
DEUTRONS
ψ1 = 0.88 mrad
1.7 mrad
ARB. UNITS
200
100
0
3.0 2.0 1.0 0 1.0 2.0 3.0
θi (mrad)

Fig. 13

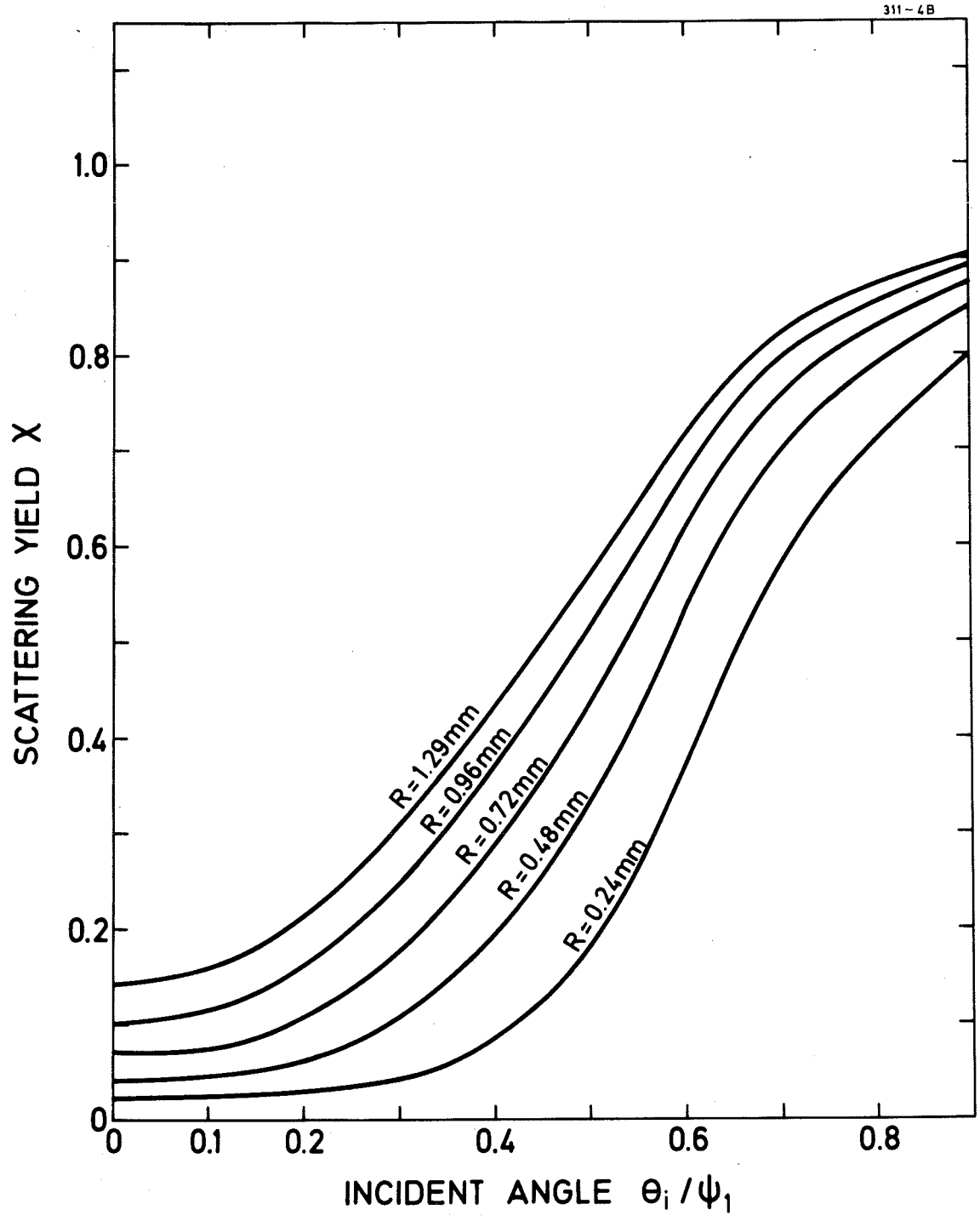
311-4B
SCATTERING YIELD X
1.0
0.8
0.6
0.4
0.2
0
0
0.1
0.2
0.4
0.6
0.8
INCIDENT ANGLE θ_i / ψ_1
R=1.29mm
R=0.96mm
R=0.72mm
R=0.48mm
R=0.24mm

Fig. 14

BLOCKING EXPERIMENT

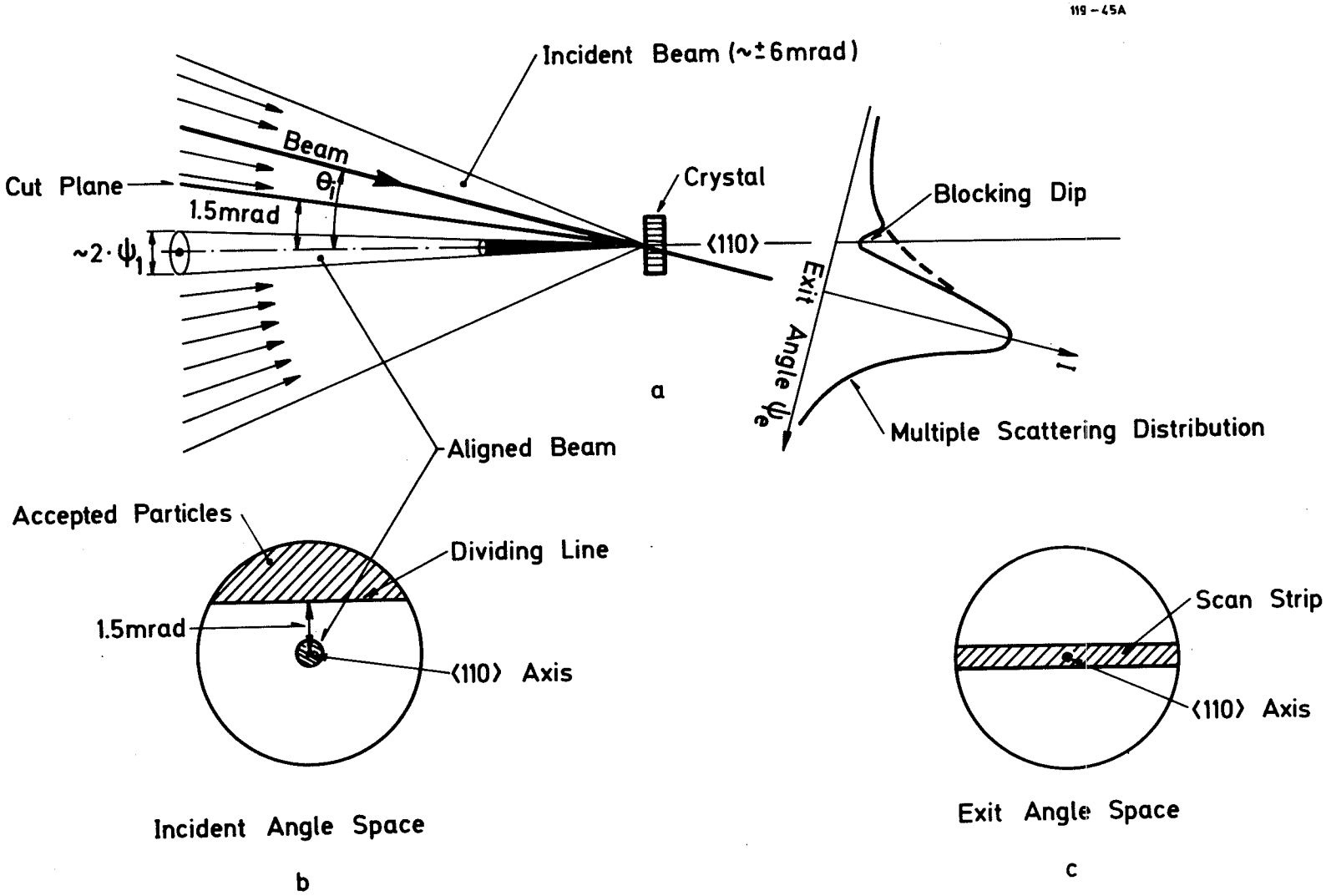

Fig. 15

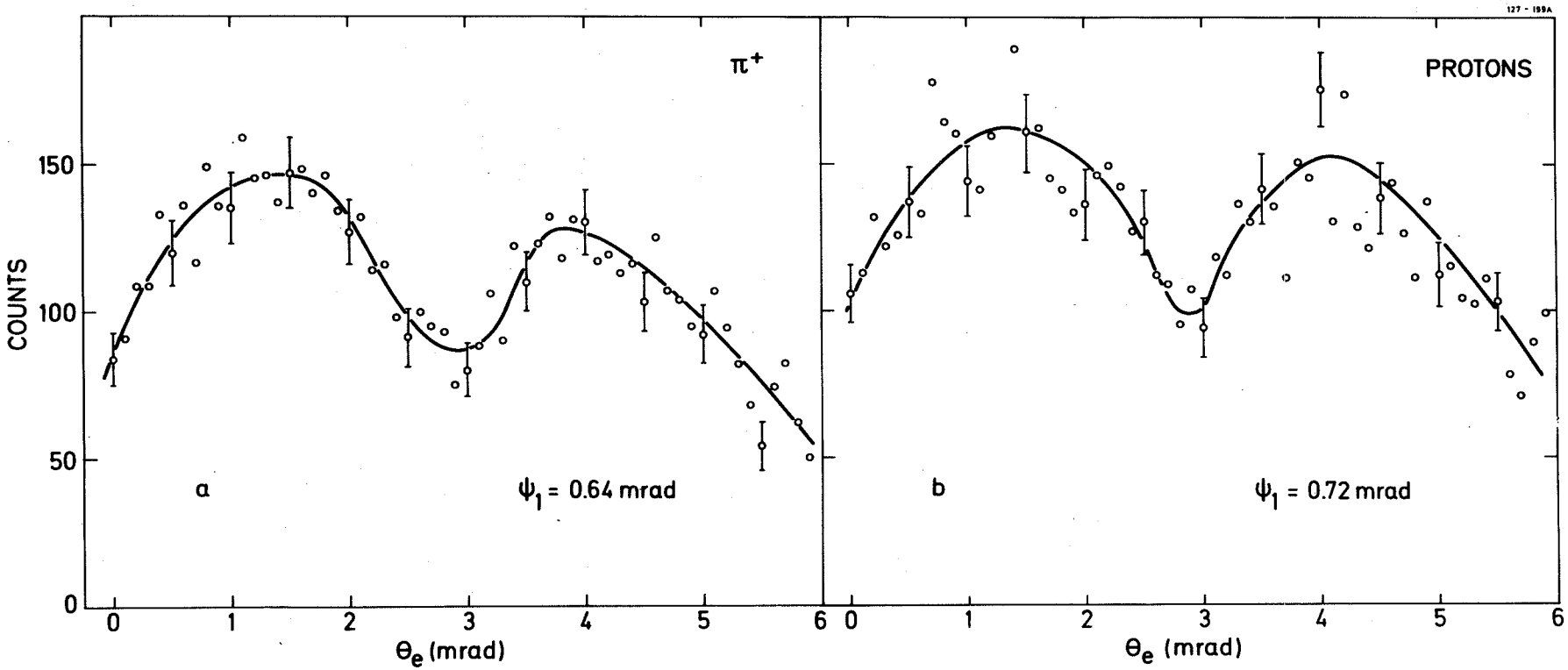
127 - 159A
π+
PROTONS
COUNTS
150
100
50
0
a
ψ1 = 0.64 mrad
b
ψ1 = 0.72 mrad
0
1
2
3
4
5
6
Θe (mrad)

Fig. 16

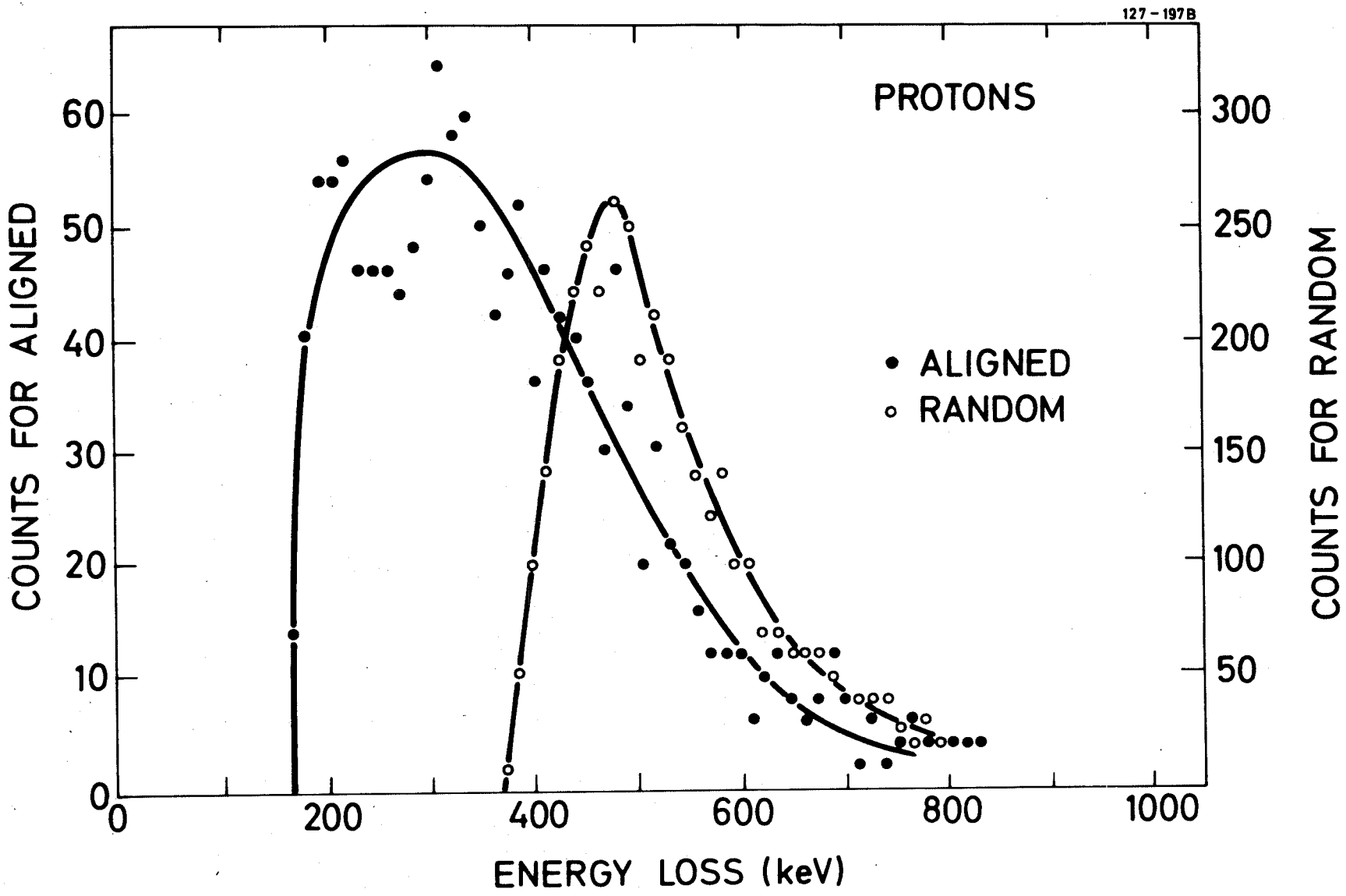
127-197B
PROTONS
ALIGNED
RANDOM
COUNTS FOR ALIGNED
COUNTS FOR RANDOM
ENERGY LOSS (keV)
0
10
20
30
40
50
60
50
100
150
200
250
300
0
200
400
600
800
1000

Fig. 17

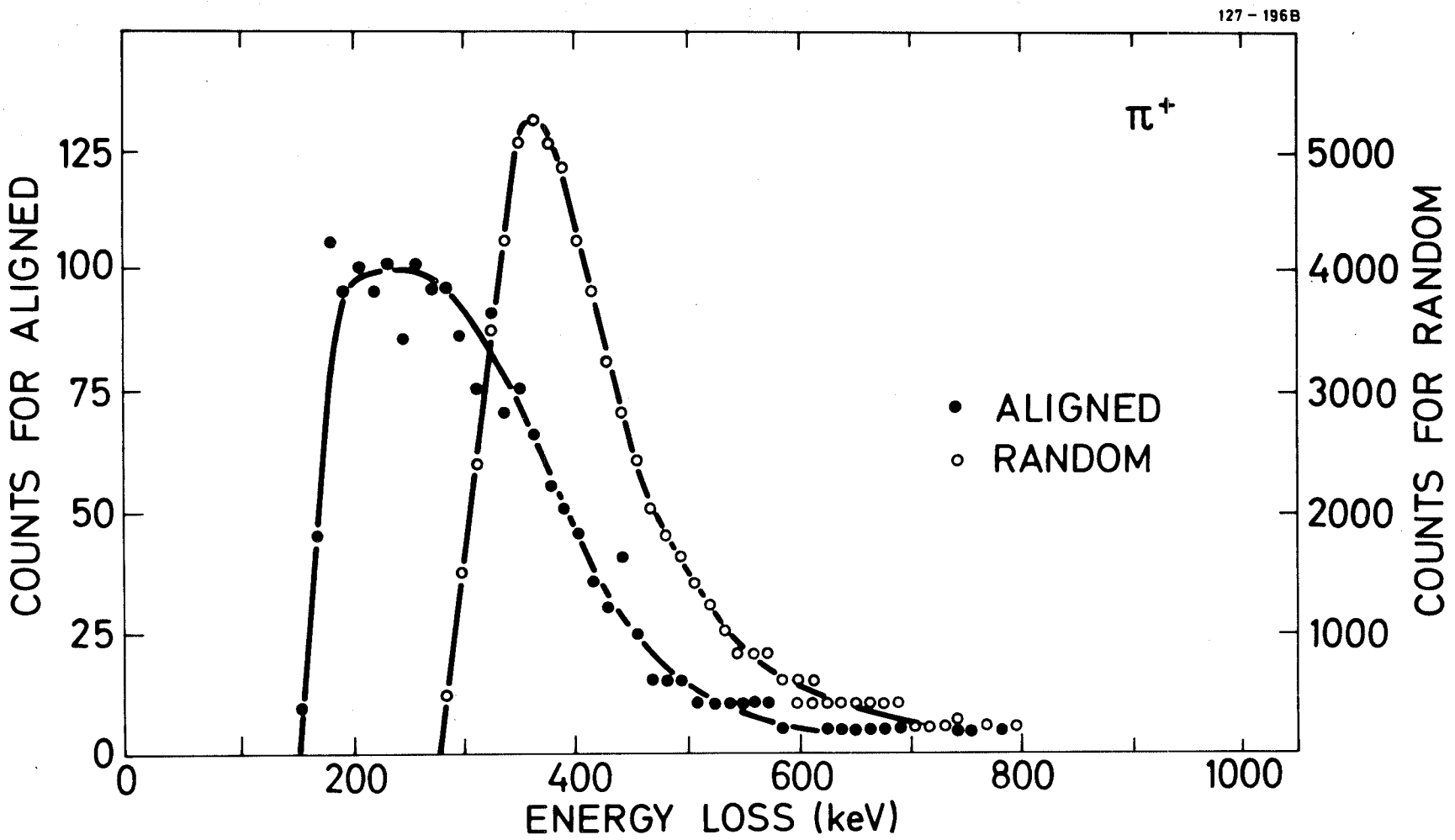
127 - 196B
π+
ALIGNED
RANDOM
COUNTS FOR ALIGNED
COUNTS FOR RANDOM
ENERGY LOSS (keV)
0
25
50
75
100
125
1000
2000
3000
4000
5000
0
200
400
600
800
1000

Fig. 18

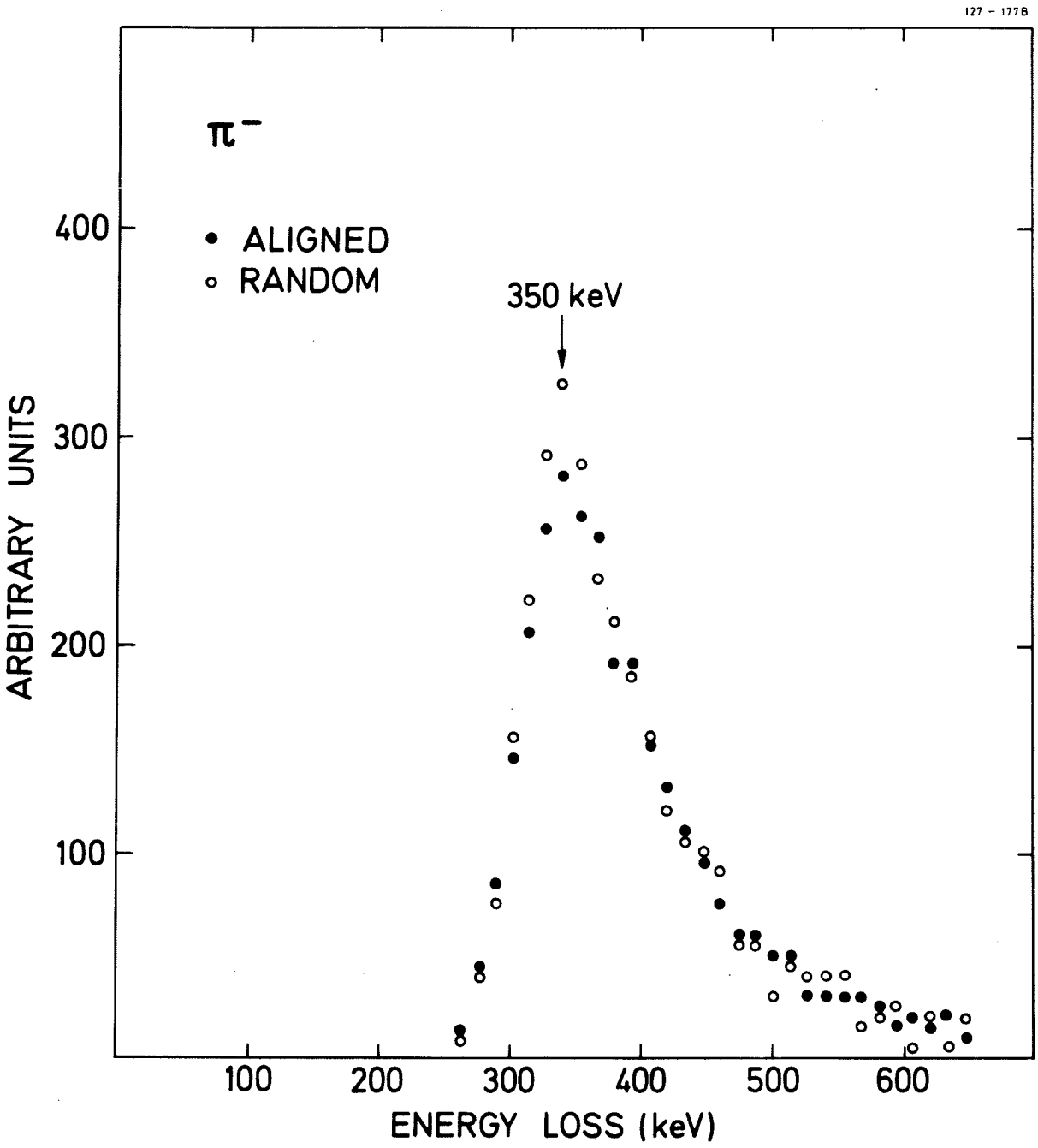
127 - 1778
π⁻
• ALIGNED
○ RANDOM
350 keV
ARBITRARY UNITS
400
300
200
100
100
200
300
400
500
600
ENERGY LOSS (keV)

Fig. 19

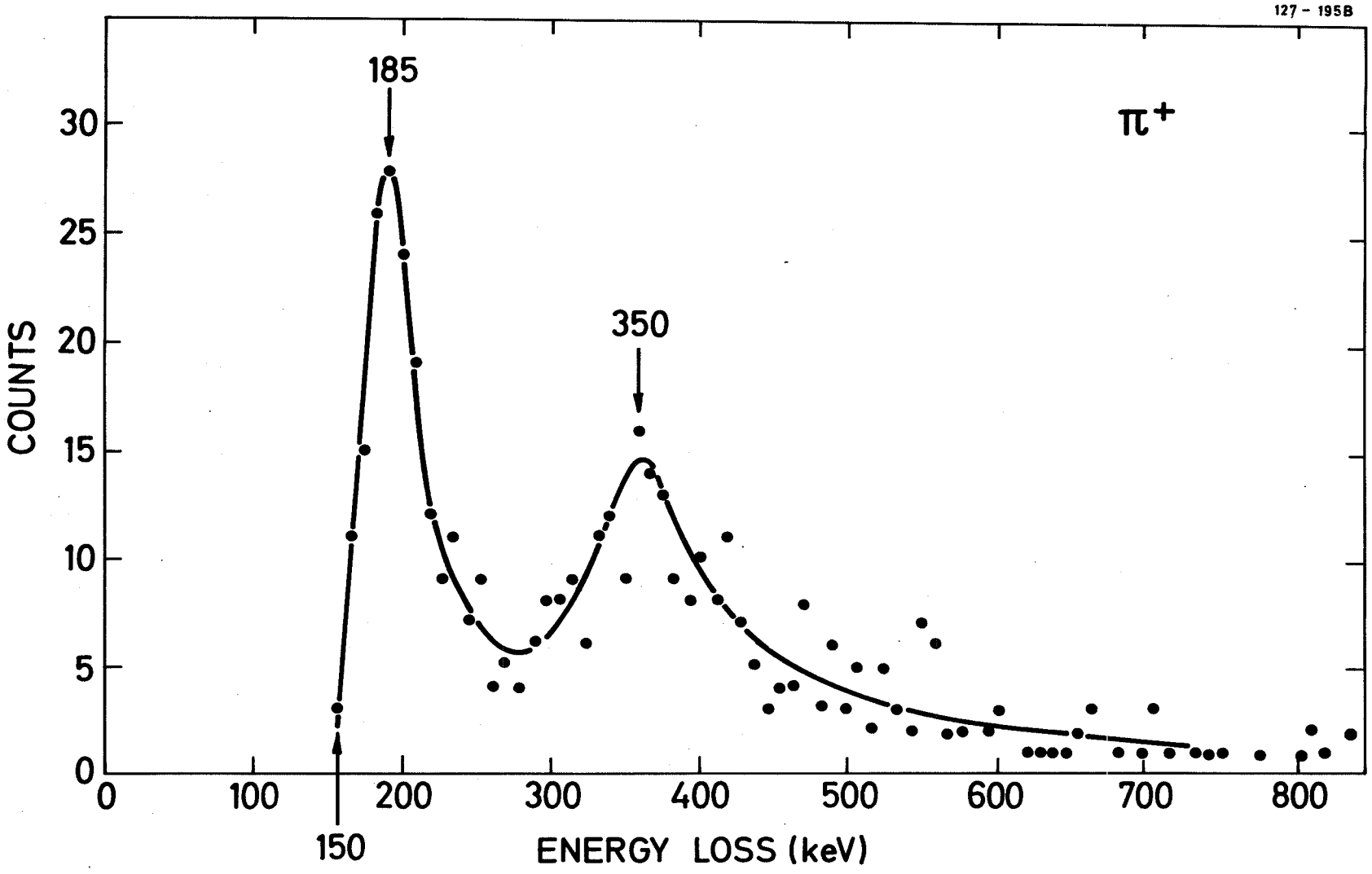
127 - 1958
185
350
150
π^+
COUNTS
ENERGY LOSS (keV)
0
5
10
15
20
25
30
0
100
200
300
400
500
600
700
800

Fig. 2o

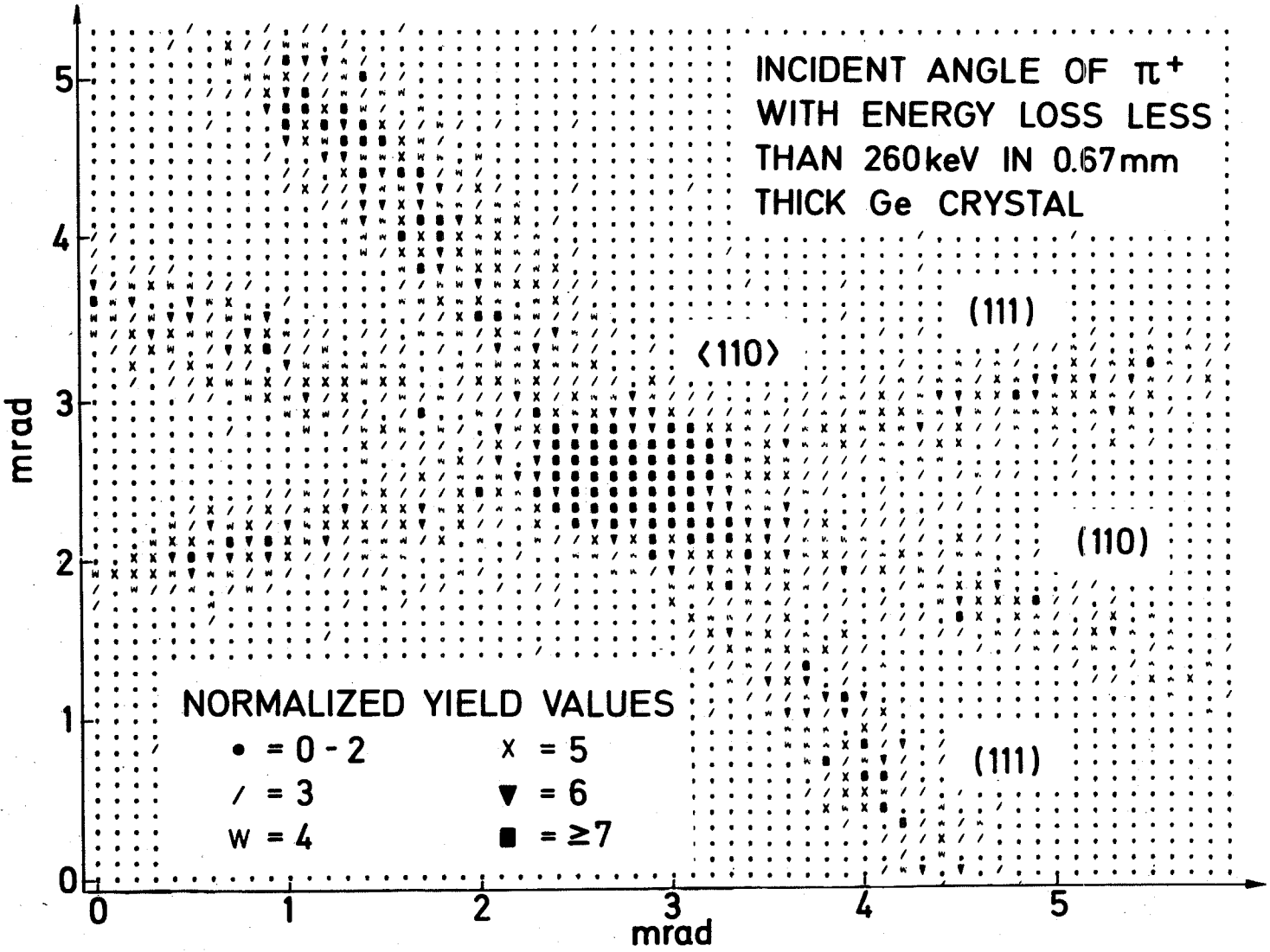
INCIDENT ANGLE OF π+
WITH ENERGY LOSS LESS
THAN 260keV IN 0.67mm
THICK Ge CRYSTAL
(111)
⟨110⟩
(110)
(111)
NORMALIZED YIELD VALUES
• = 0 - 2
x = 5
/ = 3
▼ = 6
w = 4
■ = ≥7
mrad
mrad
0
1
2
3
4
5

Fig. 21

1.35 GeV/c PROTON IN ⟨110⟩ Ge
CONTOURS OF EQUAL STOPPING (keV/mm)

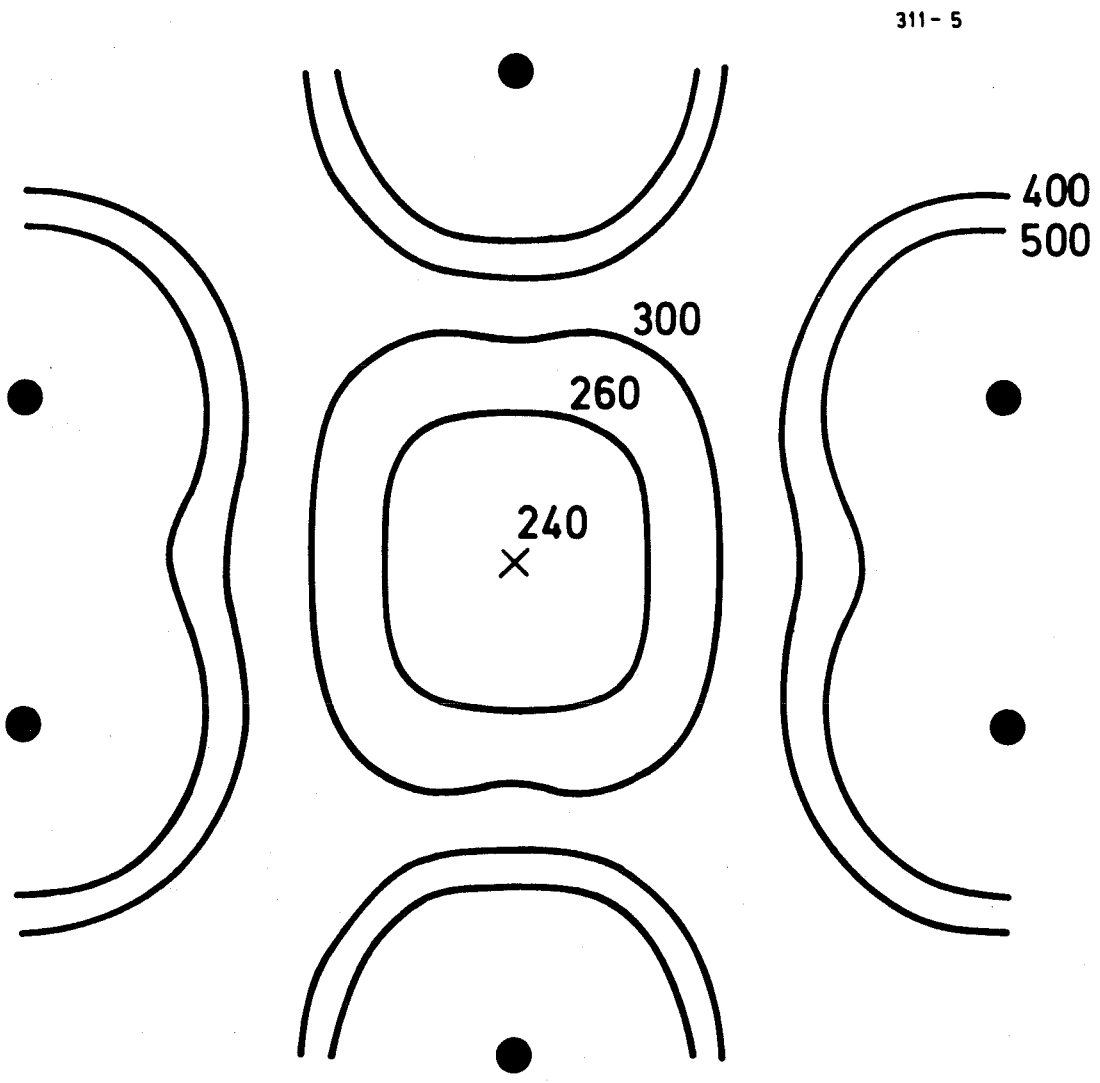

Fig. 22